Article:

Song, S.-S., Chen, J., Ye, J. orcid.org/0000-0002-6857-7450 et al. (3 more authors) (2024) Test and analysis of the interfacial bond behaviour of circular concrete-filled wire-arc additively manufactured steel tubes. Journal of Building Engineering, 82. 108171. ISSN 2352-7102

https://doi.org/10.1016/j.jobe.2023.108171

Test and analysis of the interfacial bond behaviour of circular concrete-filled wire-arc additively manufactured steel tubes

Sha-Sha Song[1], Ju Chen[1*], Jun Ye[1,2*], Guan Quan[1], Zhen Wang[3], Jianzhuang Xiao[4]

1. College of Civil Engineering and Architecture, Zhejiang University, Hangzhou, China, 310058

2. School of Civil Engineering, University of Leeds, Leeds, UK, LS2 9JT

3. Department of Civil Engineering, Hangzhou City University, Hangzhou 310015, China

4. Department of Structural Engineering, Tongji University, Shanghai, PR China

Abstract: Interfacial bond behaviour of the circular concrete-filled wire-arc directed energy deposition (DED) steel tubes was investigated experimentally, in which wire-arc DED, commonly referred to as wire-arc additive manufacturing (WAAM), represents a metal 3D printing method. Firstly, a 3D laser scanning was employed to generate the 3D models of the WAAM steel components to obtain the geometric features. A parameter relating to the surface undulation was proposed to evaluate the roughness of the WAAM steel tubes. The results of tensile testing undertaken to obtain the mechanical properties of the WAAM material were summarised. Twelve push-out specimens were tested to obtain the load-slip response and bond strength, while the influence of surface undulation, diameter-to-thickness ratio and interface length was also assessed, respectively. The test results demonstrated that: 1) after reaching the peak load, a slowly descending region appeared until a relatively stable residual load was achieved; 2) the average bond stresses of the push-out specimens were greater than those of the push-out specimens fabricated by conventional steel tubes and even checkered steel tube. Comparisons of the bond strength of the push-out specimens against existing structural design standards indicated the design guidelines of various codes were quite conservative. There needs to consider the influence of the surface undulation of the WAAM steel tube. Finally, based on the nonlinear regression of the test data generated in the present study, an empirical equation was proposed for the prediction of the average bond strength for concrete-filled WAAM steel tubes.

Keywords: Bond strength; concrete-filled steel tube (CFST); laser scanning; push-out; wire arc additive manufacturing (WAAM); 3D printing.

---

1. Introduction

Concrete-filled steel tubes (CFST) elements, have been widely applied in various construction projects, including CFST arch bridges, high-rising buildings, and CFST transmission towers [1-9]. For circular CFST subjected to the axial compressive load, their compressive strength can be improved due to the lateral confinement effect provided by the circular steel tube to the inner concrete. Most of the current research is limited to the circular CFST with conventional steel elements, in terms of experimental and numerical studies [10-18]. In addition, conventional CFSTs suffer from the challenge of low average bond strength between the steel tube and concrete [19-31]. To address this issue, concrete-filled wire-arc additive manufacturing (WAAM) steel tubes represent an innovative approach to composite structures, which has a potential to be applied in complex composite structure construction. The geometric characteristics of WAAM steel tubes are varying along the length due to the surface undulations arising from the printing process, rendering that the bond strength between the WAAM steel tube and concrete can be significantly enhanced. This strategic design allows the two materials, with distinct properties, to work together harmoniously. The steel component contributes to high tensile resistance, while the concrete element offers excellent compression capacity. By effectively utilizing the complementary characteristics of both materials, CFSTs with WAAM elements provide enhanced performance and structural efficiency.

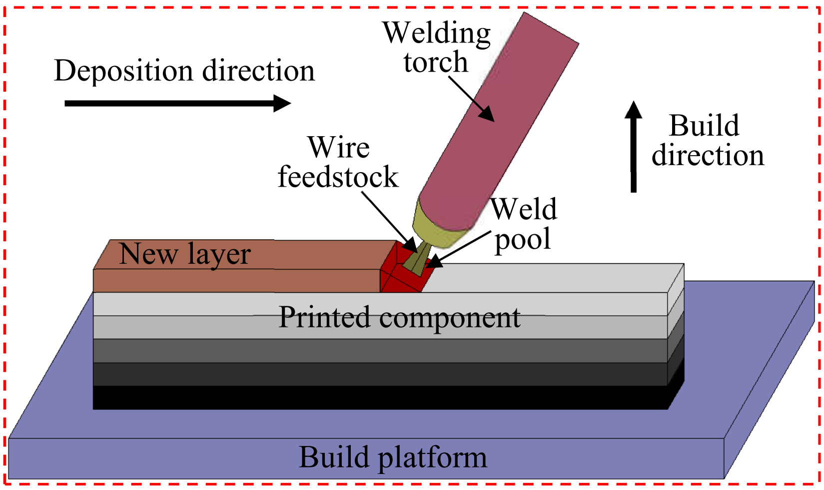

Figure 1. Schematic diagram of the WAAM process

WAAM, also known as wire-arc directed energy deposition (DED) technology, is indeed a metal 3D printing technique that has gained recognition for several notable features, including high efficiency, cost-effectiveness, flexibility in build scales, and suitability for various applications, including the construction sector [32-44]. In the WAAM process, as shown in Fig. 1, wire feedstock is melted and selectively deposited onto a substrate plate, layer by layer, until the material solidifies, and the final part is formed. Given the unique structural behaviour of WAAM components, which is beyond the scope of current design specifications [45-48], a thorough investigation was necessary for their safety assessment. To achieve this, extensive experimental and numerical studies were conducted to characterize the response of WAAM elements at the material [26,38,49-50] and cross-sectional levels [51,52], the member levels [53,54] and full structural levels [55]. The latter system level study involved the optimisation [56,57] of a series of WAAM tubular trusses. These elements were also produced using the same WAAM process employed in constructing the World's first 3D printed metal bridge [37,43,44].

Although WAAM technology has great potential for the construction industry, the extensive and successful application requires the establishment of design guidelines tailored to the manufacturing method. Currently, research on the structural behaviour of 3D printed structures has predominantly focused on structural elements produced through powder bed fusion (PBF) technology [58,59]. For WAAM structural elements, the conducted research primarily pertains to the compressive behaviour of square and circular hollow sections (SHS and CHS) components [36,51,52] and the mechanical behaviours of bolted [39-43] and T-stub [60] connections. Moreover, when it comes to CFST elements, the compressive behaviour of circular concrete-filled WAAM steel tubes has been investigated numerically and experimentally, indicating that the WAAM tubes being composed of continuously printed 'hoop', resulting in less prone to fracture. This had a positive impact on the ductility of the CFST with WAAM element after the attainment of their ultimate load [61,62], unlike CFST members fabricated from conventional steel tubes (the seam welds running along the length of fabricated tubes) where fracture of the steel tubes is often observed [63,64].

More comprehensive studies are needed to understand the structural behaviour of WAAM-produced elements in various loading conditions and configurations. The performance of CFST members relies significantly on the combined effect of the steel tube and the inner concrete, which is influenced by the interfacial bond behaviour between these components. However, the interfacial bond behaviour of CFST elements with WAAM steel tubes has not been extensively studied. To address this gap, a series of push-out tests on CFST with WAAM steel elements were conducted and presented in this study.

The manufacturing process of the WAAM CHS and oval steel tube was first presented. The methods adopted for the determination of as-built geometric properties of the examined specimens, featuring hand measurements and 3D laser scanning, are described. A factor of surface undulation was proposed to evaluate the roughness of the WAAM steel tube. The results of complementary material tests, undertaken for the determination of the mechanical properties of the concrete and WAAM material were then summarised. A detailed description of the push-out tests on the CFST specimens was provided, while the test results are analysed and discussed. The influence of the factor of surface undulation, diameter-to-thickness ratio and interface length was also presented. Comparisons between the bond strength of the push-out specimens and existing structural design standards [46,65-67] highlighted the need to consider the effects of the surface undulations of the WAAM steel tube. Finally, based on the nonlinear regression of the test data generated in the present study, an empirical equation was proposed for predicting the average ultimate bond strength for concrete-filled WAAM steel tubes.

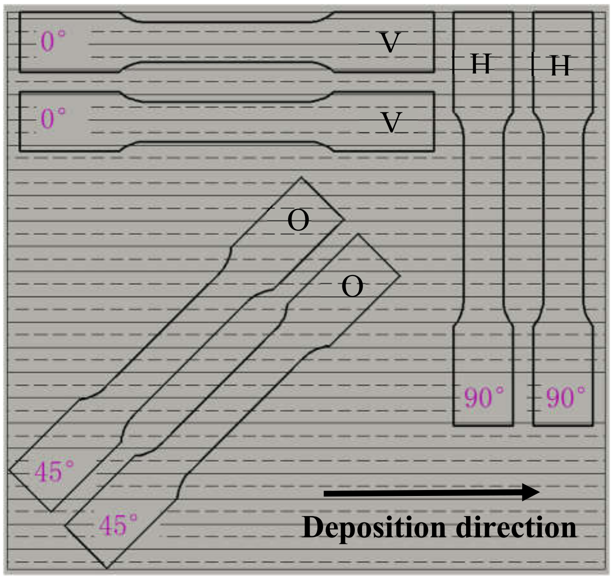

(a) Orientation of tensile coupons extracted from WAAM oval tube

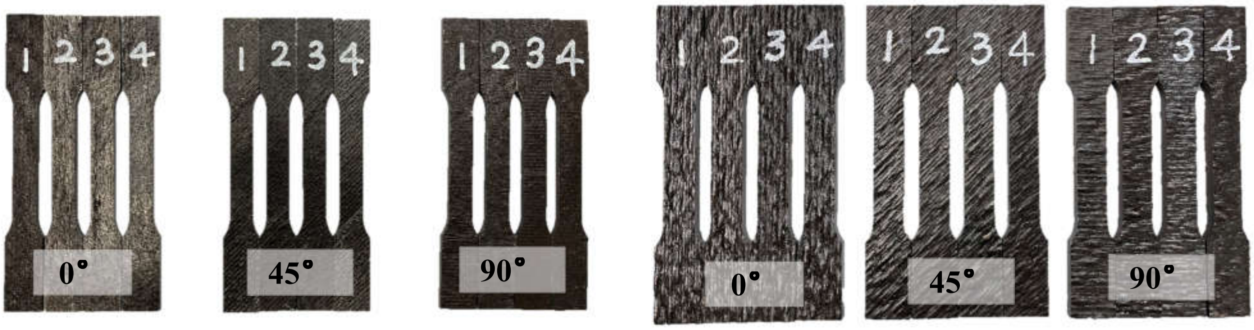

(b) 4 mm coupons (c) 8 mm coupons

Figure 2. Orientation of tensile coupons relative to deposition direction

2. WAAM Steel Component

2.1. Production

A total of twelve push-out test specimens were fabricated with varying nominal diameters (150 mm, 180 mm, 210 mm, and 240 mm) and lengths (300 mm, 400 mm, and 500 mm). These tubes were manufactured with two different nominal thicknesses (4 mm and 8 mm), resulting in nominal diameter-to-thickness ratios ranging from 18 to 60. Additionally, two oval steel tubes with flat sides were also produced, with nominal thickness of 4 mm and 8 mm, respectively. These oval tubes were used for extracting planar elements to create tensile coupons. To label the WAAM steel tubes, a symbol system was defined based on the length, diameter, and thickness of the specimens. As an illustration, the label "L300D150T4" indicates that the WAAM steel tube with a nominal length, diameter, and thickness of 300 mm, 150 mm, and 4 mm, respectively. Similarly, the labelling for the tensile coupons utilizes the first letters of "horizontal" (90° to the deposition direction), "vertical" (0° to the deposition direction) and "oblique" (45° to the depositions direction) as the start of the specimen's name. For instance, the label "O4-1" represents the first oblique tensile coupon with a thickness of 4 mm, extracted from the WAAM oval steel tube at a 45° angle to the deposition direction - see Fig. 2.

(a) Printing of a subset of the WAAM CHS steel tubes

(b) Printed CHS steel tubes

Figure 3. Printing equipment and printed components of WAAM

Fig. 3(a) illustrates the printing process of a selected subset of WAAM CHS steel tubes. The WAAM components were produced utilizing a welding torch connected to a six-axis robotic arm and a metal inert gas (MIG) welding machine. A shielding gas mixture of 98% Ar and 2% CO_2 was utilized during the process. The key process parameters applied during WAAM are summarized in Table 1. The environmental conditions of the motor room, including temperature and humidity, ranged from 12 °C to 21 °C and 50% to 65%, respectively. The printing process involved layer-by-layer fabrication, following the cross-section slice traces defined in their as-design models created in Rhino 3D [68]. Carbon steel welding wire ER70S-6 was used as the feedstock material, and it was deposited onto a substrate plate made of Q235 steel grade. After fabrication, the WAAM CHS and oval steel tubes were separated from their build platform using a plasma arc cutter. Subsequently, both ends of the WAAM steel tubes were machined to be flat and parallel, while their exterior surfaces were subjected to sandblasting with glass beads to eliminate any welding residue from the WAAM process, as shown in Fig. 3(b).

2.2. Geometric Properties

2.2.1. Geometrical Measurements

In contrast to conventionally produced CHS steel tubes, the geometric characteristics of the WAAM steel tubes, such as wall thickness and inner and outer diameters, were varying along the tube length due to the undulations of WAAM surface. Consequently, conventional measuring techniques were deemed impractical for assessing these variations. To obtain the as-built geometric properties of the WAAM steel tubes, two measuring techniques were employed: the hand measurements and 3D laser scanning.

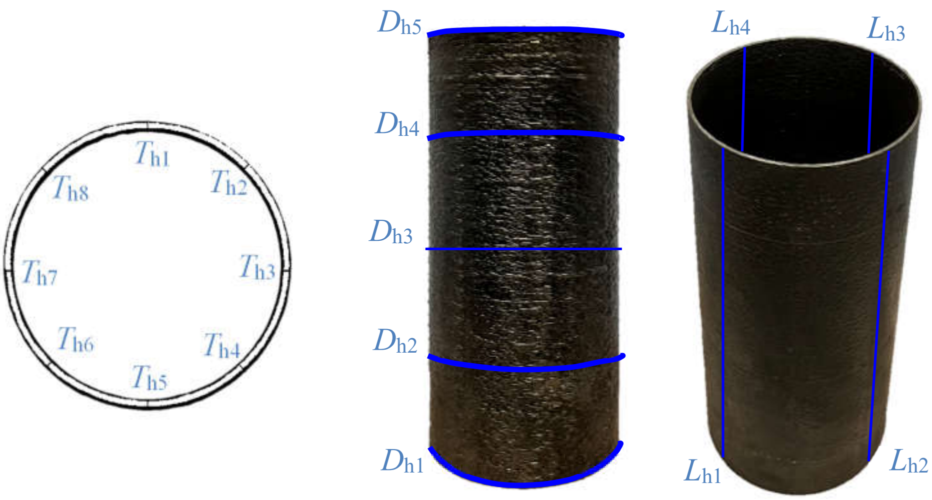

Figure 4. Locations of hand measurement of WAAM CHS steel tubes

Table 1 Process parameters used for WAAM specimens

Nominal thickness (mm)	Welding speed (m/min)	Wire feed rate (m/min)	Deposition rate (kg/h)	Wire feedstock diameter (mm)	Current (A)	Arc voltage (V)	Layer thickness (mm)
4	0.6	2.3	1.2	1.2	75	19.6	1
8	0.3	4.0	2.1	1.2	110	21.3	2.1

Table 2 Measured average geometric properties of WAAM steel tubes

Steel tubes	L_n (mm)	D_n (mm)	T_n (mm)	L_h (mm)	D_h (mm)	T_h (mm)	$m_{Hand,T}$ (kg)	L_{Scan} (mm)	D_{Scan} (mm)	T_{Scan} (mm)	$A_{Scan,T}$ (mm^2)	$V_{Scan,T}$ (mm^3)	ρ (kg/m^3)	$\frac{V_{Scan,T}}{V_{Hand,T}}$
L300D150T4	300	150	4	318.5	152.38	4.13	4.69	317.2	152.42	4.03	1879.10	598891.39	7831.14	0.98
L300D150T8	300	150	8	317.0	157.72	7.96	9.16	317.5	155.93	7.95	3697.08	1176008.34	7789.06	0.99
L300D180T4	300	180	4	301.0	185.57	3.98	5.36	301.8	182.36	4.07	2281.51	690741.96	7759.77	1.01
L300D180T8	300	180	8	304.5	187.72	7.81	10.43	304.6	185.69	7.86	4394.13	1343527.41	7763.15	1.00
L400D180T4	400	180	4	417.0	183.82	3.99	7.30	416.9	182.15	3.99	2232.47	931959.45	7832.96	0.99
L400D180T8	400	180	8	400.0	187.48	7.87	13.81	399.9	185.73	7.91	4426.17	1769881.45	7802.78	1.00
L400D210T4	400	210	4	408.0	214.14	3.98	8.46	406.8	212.39	4.08	2669.59	1088272.20	7773.79	1.02
L400D210T8	400	210	8	403.9	217.25	7.73	16.03	403.9	215.43	7.80	5095.09	2063459.81	7768.51	1.00
L500D210T4	500	210	4	525.0	213.75	4.10	10.88	524.3	212.13	4.10	2677.96	1407695.08	7728.95	0.99
L500D210T8	500	210	8	495.0	216.77	7.78	19.81	499.8	215.29	7.78	5073.60	2537803.17	7805.96	1.00
L500D240T4	500	240	4	519.0	243.51	4.14	12.29	518.8	241.99	4.17	3113.16	1568762.48	7834.20	0.97
L500D240T8	500	240	8	520.0	247.22	7.81	23.44	520.5	244.92	7.66	5712.01	2980750.80	7863.79	0.98
												Mean	7796.17	0.99
												CoV	0.005	0.014

Table 3 Measured average geometric properties of WAAM steel coupons

Coupons			b_n (mm)	t_n (mm)	$m_{Hand,C}$ (g)	b_{Scan} (mm)	t_{Scan} (mm)	$A_{Scan,C}$ (mm^2)	$V_{Scan,C}$ (mm^3)	A (mm^2)	$\frac{A}{A_{min}}$	$\frac{A}{A_{max}}$	ρ (kg/m^3)
As-built	0°	V4-1	12.5	4	71.44	12.54	3.52	44.14	9137.49	44.14	1.02	0.97	7818.34
	0°	V4-2	12.5	4	71.33	12.60	3.69	46.51	9130.70	46.51	1.03	0.97	7812.11

0°	V4-3	12.5	4	71.52	12.55	3.49	43.81	9060.84	43.81	1.04	0.95	7893.31
0°	V4-4	12.5	4	71.01	12.61	3.47	43.76	9123.80	43.76	1.02	0.98	7782.94
45°	O4-1	12.5	4	71.51	12.49	3.46	43.22	8996.14	43.22	1.03	0.96	7948.96
45°	O4-2	12.5	4	71.51	12.51	3.48	43.55	9070.98	43.55	1.02	0.98	7883.38
45°	O4-3	12.5	4	71.32	12.50	3.49	43.61	9039.69	43.61	1.01	0.98	7889.65
45°	O4-4	12.5	4	71.23	12.44	3.45	42.91	8846.96	42.91	1.03	0.97	8051.35
90°	H4-1	12.5	4	71.57	12.47	3.52	43.88	9198.05	43.88	1.04	0.97	7781.00
90°	H4-2	12.5	4	70.98	12.51	3.49	43.67	8953.09	43.67	1.05	0.90	7927.99
90°	H4-3	12.5	4	70.75	12.40	3.47	43.03	8941.76	43.03	1.02	0.94	7912.31
90°	H4-4	12.5	4	71.77	12.52	3.40	42.58	8887.80	42.58	1.03	0.98	8075.11
0°	V8-1	20	8	339.16	20.00	8.41	168.20	43333.39	168.20	1.03	0.97	7826.76
0°	V8-2	20	8	338.02	20.04	8.30	166.31	42664.20	166.31	1.04	0.95	7922.80
0°	V8-3	20	8	341.67	19.98	8.55	170.87	44079.91	170.87	1.05	0.96	7751.15
0°	V8-4	20	8	342.86	19.99	8.53	170.48	43974.16	170.48	1.04	0.95	7796.85
45°	O8-1	20	8	333.38	20.00	8.24	164.77	42779.89	164.77	1.03	0.96	7792.91
45°	O8-2	20	8	334.89	19.95	8.13	162.18	42160.94	162.18	1.06	0.94	7943.13
45°	O8-3	20	8	330.89	19.80	8.30	164.30	42477.53	164.30	1.05	0.95	7789.77
45°	O8-4	20	8	331.50	19.88	8.25	163.99	42289.52	163.99	1.04	0.96	7838.82
90°	H8-1	20	8	334.47	20.00	8.33	166.62	42959.95	166.62	1.06	0.92	7785.62
90°	H8-2	20	8	338.14	19.95	8.35	166.62	43021.73	166.62	1.05	0.93	7859.75
90°	H8-3	20	8	339.23	19.97	8.35	166.75	43329.01	166.75	1.04	0.92	7829.17
90°	H8-4	20	8	338.71	20.02	8.34	166.99	43130.41	166.99	1.06	0.96	7853.16
											Mean	7865.26
											CoV	0.011

(1) Hand Measurement

A digimatic micrometre of 0.001 mm accuracy and a measuring tape were employed to provide baseline geometric data for the WAAM steel tubes, the wall thickness T_h was determined as the average value of eight measurements taken at eight locations equally spaced along the section diameter, utilising the digimatic micrometre-as shown in Fig. 4. Similarly, measurements of the perimeter C_h of the outer surface of each steel tube were taken at five locations evenly distributed along the member length, and their mean value was used to determine the average outer diameter D_h. Finally, the length L_h of each steel tube was determined based on four length measurements, taken at the locations indicated in Fig. 4. In addition, an electronic balance was used to weigh the WAAM tensile coupons and tubes (with their messes labelled $m_{\text{Hand,C}}$ and $m_{\text{Hand,T}}$), in order to determine the density ρ of the WAAM components, in line with Eq. (1). The average geometric properties of the steel tubes as determined by the hand measurements are listed in Tables 2 and 3, where $V_{\text{Hand,T}}$ is the volume calculated using the measured values.

$$\rho = \frac{m_{\text{Hand}}}{V_{\text{Scan}}} \tag{1}$$

(2) 3D Laser Scanning

A 3D laser scanning was employed to capture the digital geometry of the WAAM steel components, in order to obtain an accurate and detailed replication surface morphology prior to testing. A SCANTECH 3D laser scanner, capable of capturing up to 500,000 points per second with an accuracy of 0.05 mm, was employed to scan all the WAAM steel tubes and coupons - see Fig. 5(a). Following calibration of the scanner (see Fig. 5(b)), markers were attached to the surfaces of the WAAM steel tubes and base plate, respectively, to facilitate alignment of the relative coordinate systems of the 3D point clouds during the coordinate conversion process, as shown in Fig. 6. After scanning, the point cloud data were processed by the computer scan software. The morphology of the overall surface of each WAAM component was obtained by merging the different scan views acquired, using the mutual red markers between adjacent scans - see Fig. 6. Merging of the different point clouds was operated based on point cloud registration, whereby the coordinates of all data points were transformed from their initial individual coordinate systems into a common global coordinate system.

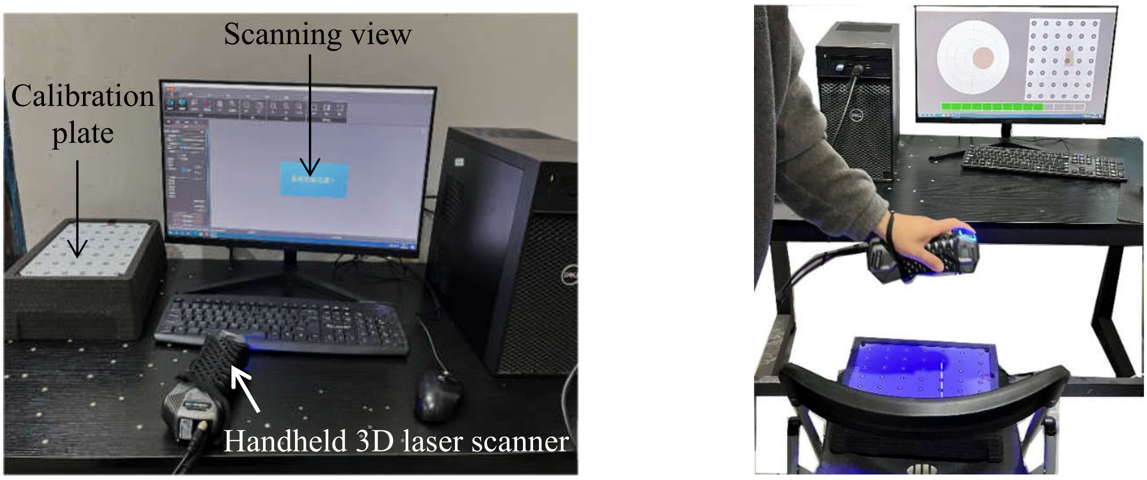

(a) Handheld 3D laser scanner (b) Calibration of the scanner

Figure 5. SCANTECH 3D laser scanner

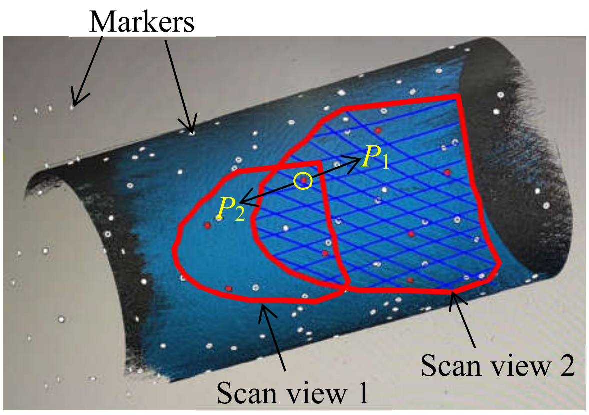

Figure 6. Scanning principle

For the WAAM tensile coupons, the surface profile was obtained with one continuous scan, as shown in Fig. 7 (a). The acquisition spacing of the captured 3D points was 0.05 mm for the WAAM steel coupons. For the WAAM steel tube, the outer surface profile of the steel tubes was scanned with one continuous scan, as shown in Fig. 7 (b), while the inner surfaces at both tube ends were scanned separately, and then merged to form the complete inner surface, as shown in Fig. 8. The acquisition spacing of the captured 3D points was 0.2 mm for the WAAM steel tubes.

Typical comparisons between the scanned surface morphologies and the corresponding WAAM components are shown in Fig. 9. The scanned 3D models (.stl) were subsequently imported into the software of Geomagic Wrap [69], where the scanned point cloud was optimized, de-noised and the grid processed to form a 3D surface in the software again. Any possible holes in the surface were patched to form a closed 3D surface model (.stl), for determination of its volume. Note that the volumes of the WAAM steel tubes $V_{San,T}$ and of the steel coupons $V_{San,C}$ were determined based on the laser scans and are presented in Tables 2 and 3, respectively. Following a closed 3D surface model formed, the grid files were imported into the software of Rhino 3D [68], while the detailed geometric dimensions of the WAAM components were determined. The average values of D_{Scan}, T_{Scan} and $A_{Scan,T}$, along with the column length L_{Scan} of each steel tube are listed in Table 2. Meanwhile, the average values of b_{Scan}, t_{Scan} and $A_{Scan,T}$ for the typical section of each coupon are listed in Table 3.

(a) Coupon specimens (b) Typical steel tube

Figure 7. 3D laser scanning of the specimens

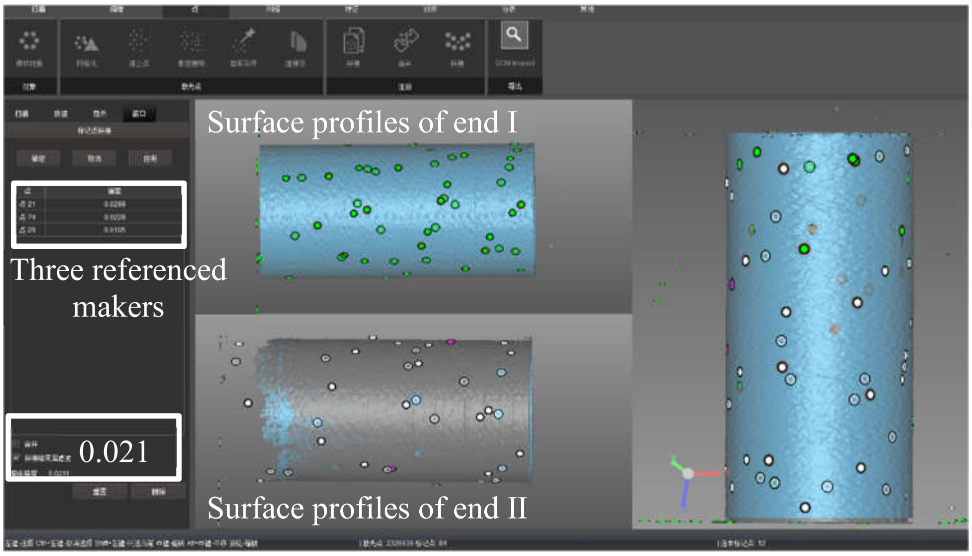

Figure 8. Merging the inner surface of both tube ends

2.2.2. Comparison

The measured volumes of the WAAM steel tubes obtained by hand measurements and 3D laser scanning are compared in Table 2. The volumes measured by hand $V_{Hand,T}$ was similar to the volume $V_{Scan,T}$

determined by the laser scans with the mean value of the $V_{\text{Scan,T}}/V_{\text{Hand,T}}$ ratio being 1.00 and the coefficient of variation (CoV) being 0.012, providing verification of the 3D laser scanning method. Overall, the 3D laser scanning method was considered the most suitable for obtaining accurate measurements of the detailed geometric dimensions of WAAM steel components. The hand measurements could be used as references for engineering design.

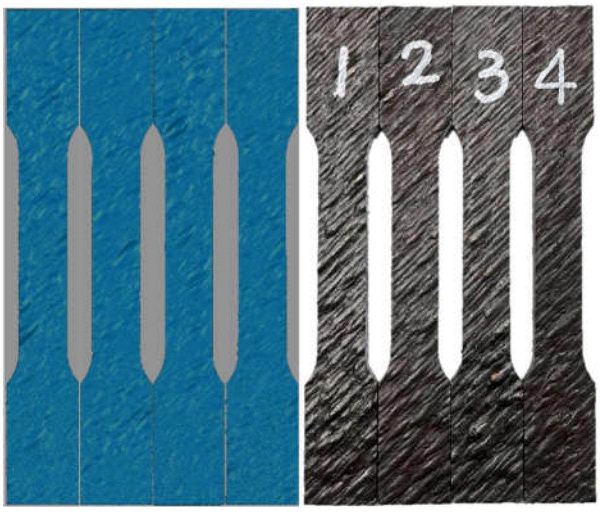

(a) Coupons

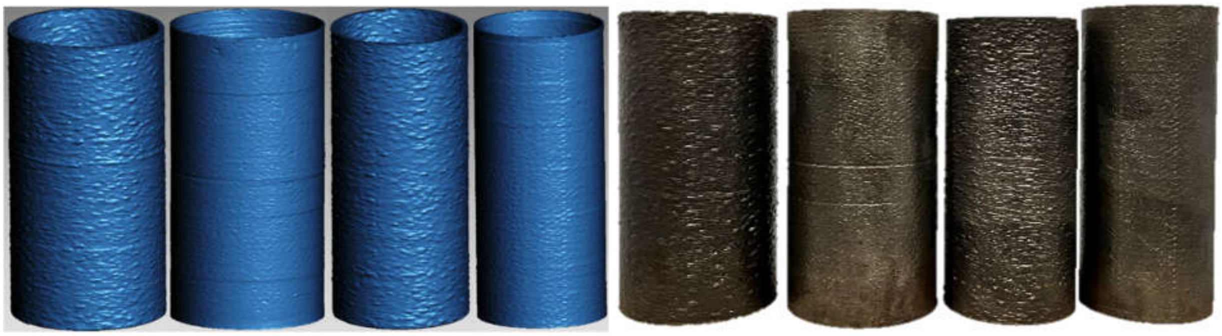

(b) Steel tubes

Figure 9. Comparisons of scanned surface profiles with respective specimens

2.2.2. Determination of Cross-sectional Dimensions

The 3D models of the WAAM steel components obtained by the laser scans were imported into Rhino 3D [68] for geometric analysis. Contouring of each component along its length was first undertaken to accurately obtain its cross-sectional dimensions. Contours of typical WAAM components in Rhino 3D is shown in Fig. 10. A sensitivity study was undertaken to determine the most suitable contour spacing for the examined WAAM steel components. Typical WAAM components (considering the influence of different deposition directions and thicknesses), were contoured with the spacing of 2.0 mm, 1.0 mm, 0.5 mm, 0.2 mm and 0.1 mm and their cross-sectional area was subsequently determined. The obtained results are shown in Fig. 11, in which the mean, minimum and maximum values of the cross-sectional areas (A, A_{min} and A_{max}) obtained from the different contour spacings were normalised against the corresponding values from a contour spacing dx=0.1 mm. It is shown that the values of A_{min} and A_{max} were sensitive to the contour spacing compared to the mean value of A. A value of dx=0.2 mm was adopted for the conducted geometric analyses. It should be noted that the spacing of 0.2 mm was still smaller than the WAAM layer thickness, which was approximately 2.1 mm for the 8 mm thick component and 1.0 mm for the 4 mm thick component.

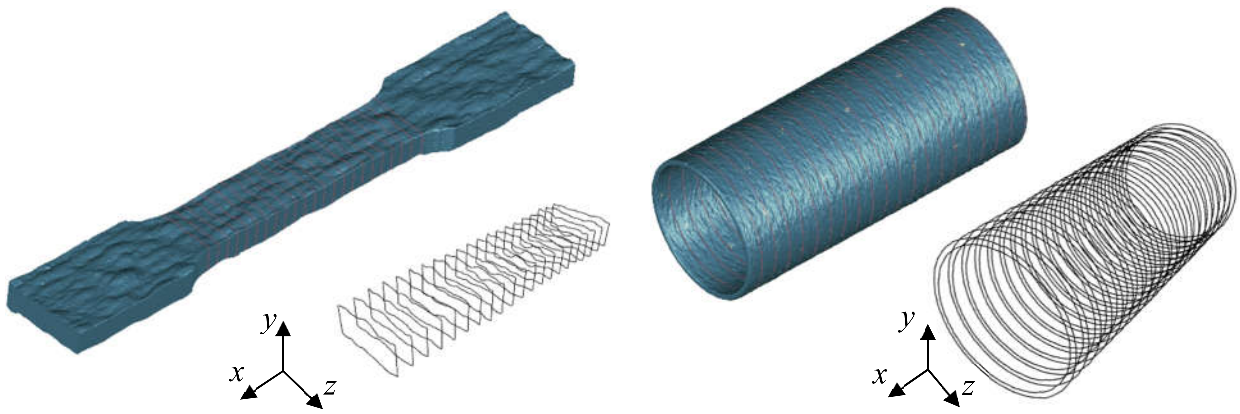

(a) WAAM steel coupon (b) WAAM steel tube

Figure 10. Scanned 3D model and cross-sectional contours of typical WAAM steel components

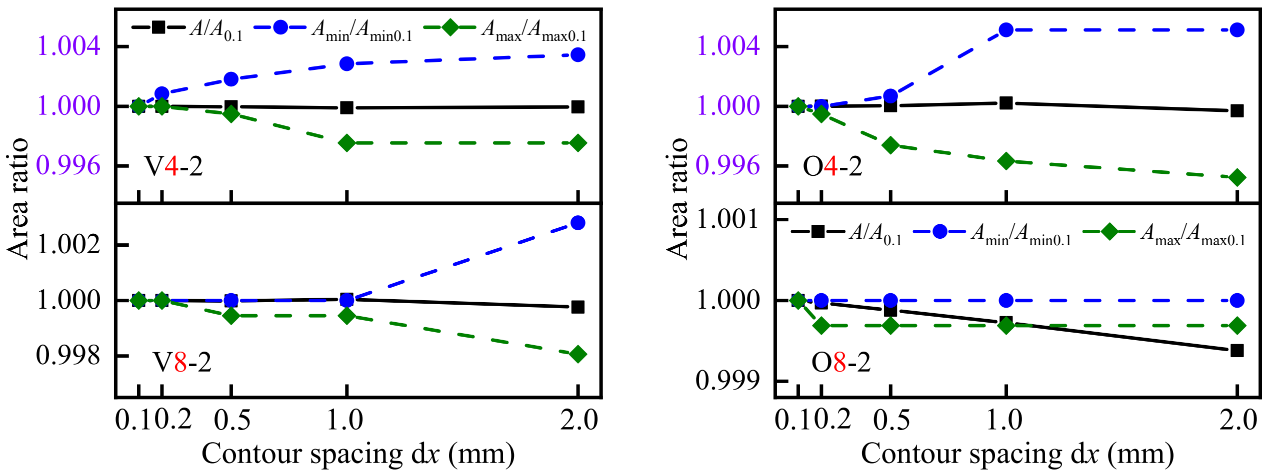

(a) Tensile coupons at 0° to the deposition direction

(b) Tensile coupons at 45° to the deposition direction

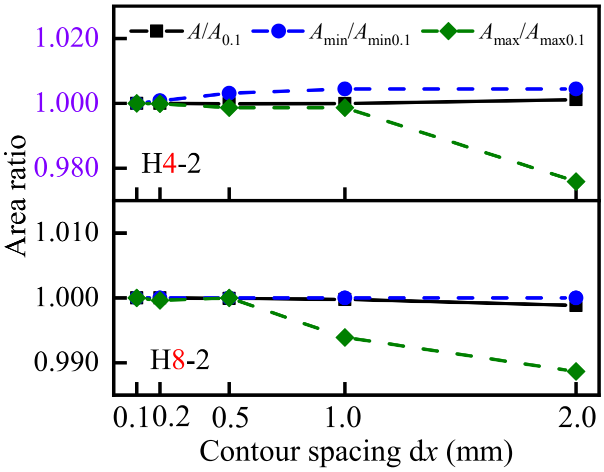

(c) Tensile coupons at 90° to the deposition direction

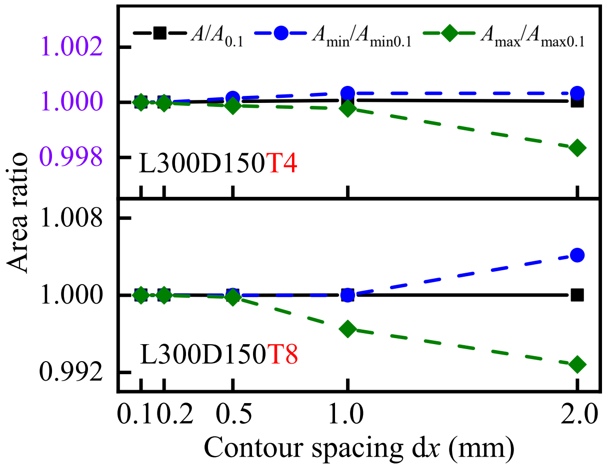

(d) WAAM steel tube

Figure 11. Results of sensitivity analysis on contour spacing d*x*

Tables 3 and 4 present a summary of the geometric properties of the WAAM steel tubes. where T, D and L are the mean values of the wall thicknesses, outer diameter and length of the WAAM steel tubes, respectively; and A, A_{min} and A_{max} are the mean, minimum, and maximum values of the cross-sectional areas.

Table 4 Summary of the geometric properties of the WAAM steel tubes as determined by the laser scans

WAAM steel components	L (mm)	D (mm)	T (mm)	A (mm^2)	$\frac{A}{A_{min}}$	$\frac{A}{A_{max}}$	ζ_{su}
L300D150T4	317.2	152.42	4.03	1879.10	1.06	0.95	0.36
L300D150T8	317.5	155.93	7.95	3697.08	1.06	0.89	0.95
L300D180T4	301.8	182.36	4.07	2281.51	1.05	0.95	0.17
L300D180T8	304.6	185.69	7.86	4394.13	1.03	0.97	0.72
L400D180T4	416.9	182.15	3.99	2232.47	1.03	0.96	0.14
L400D180T8	399.9	185.73	7.91	4426.17	1.08	0.95	1.31
L400D210T4	406.8	212.39	4.08	2669.59	1.03	0.97	0.15
L400D210T8	403.9	215.43	7.80	5095.09	1.05	0.82	1.30
L500D210T4	524.3	212.13	4.10	2677.96	1.04	0.96	0.13
L500D210T8	499.8	215.29	7.78	5073.60	1.04	0.96	0.66
L500D240T4	518.8	241.99	4.17	3113.16	1.04	0.96	0.27
L500D240T8	520.5	244.92	7.66	5712.01	1.03	0.89	0.92

2.3. Factors of Surface Undulation

Tables 3 and 4 provide comparisons between the values of the mean to minimum and mean to maximum cross-sectional areas (i.e., A/A_{min} and A/A_{max}). The distribution of normalised cross-sectional areas A_i/A along with the component longitudinal length for typical tensile coupons and steel tubes is shown in Fig.

12. It can be seen that the surface undulations of the WAAM steel components were substantial, especially for the thicker WAAM steel tube. Geometric undulations could be observed in the specimen surface of the WAAM steel component as illustrated in Fig. 13. Furthermore, it can be observed that the maximum difference between the average cross-sectional areas of the WAAM steel tubes within a longitudinal length of 100 mm at both ends and the average cross-sectional area of the entire steel tube did not exceed 3%. This suggests that surface morphology within a length range of 100 mm at both ends could provide a good estimation with reasonable accuracy.

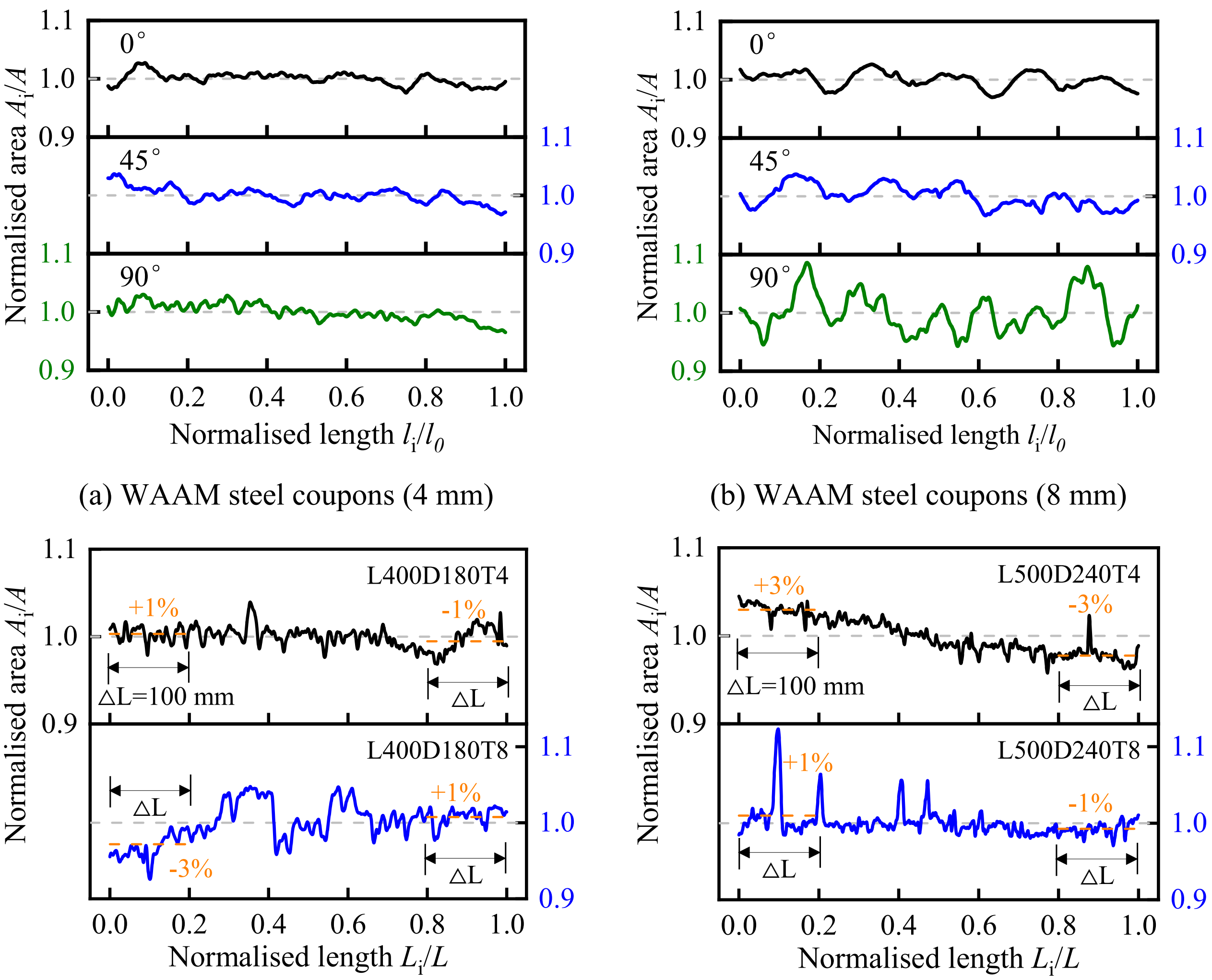

(a) WAAM steel coupons (4 mm) (b) WAAM steel coupons (8 mm)

(c) WAAM steel tubes (L400D180T4 and L400D180T8) (d) WAAM steel tubes (L500D240T4 and L500D240T8)

Figure 12. Distribution of normalised areas A_i/A along with the component length

Since the surface geometric undulation of the WAAM steel tube is related to the statistical cross-sectional area of the steel tube, it is necessary to analyse the variation of the cross-sectional area along the length of the WAAM steel tubes (see Fig. 14) to assess the effects of geometric undulations on their surface both qualitatively and quantitatively. It can be observed that, except for the L300D180 series, the statistical dispersion of the normalized cross-sectional area of these WAAM steel tubes is positively correlated with their thickness, indicating that the greater the thickness of these WAAM steel tube, the more pronounced the statistical dispersion of its normalized cross-sectional area. In addition, from the actual morphology of the steel tube surface shown in Fig. 13, it is evident that for the WAAM steel tubes in this paper, the geometric undulations of the surface of the WAAM steel tubes become more prominent as the tube thickness increases. This is due to the thicker printed layer T_y in thicker steel tubes (T_y=2.1 mm for 8 mm thick steel tubes and T_y=1 mm for 4 mm thick steel tubes - see Table 1), which results in significant geometric undulations on the surface of the WAAM steel tube. Furthermore, as illustrated in Fig. 15, the deposition diagram during the printing process reveals that the surface geometric undulations of the WAAM steel tube are also influenced by their diameter. It can be seen that for WAAM steel tubes with different diameters, the lengths of the surface deposited during the same printing time are denoted as $\Delta l_1=v_1 t$ and $\Delta l_2=v_2 t$, respectively, where v_1 and v_2 represent the welding speed of the WAAM process. If the thicknesses of the printed steel tubes are the same, then v_1 equals v_2 (as mentioned in Table 1), which means $\Delta l_1=\Delta l_2$ (i.e., for WAAM steel tubes with the same thickness, the deposition lengths of the welding gun are equal during the same printing time). Therefore, for WAAM steel tubes with the same thickness and welding speed but different diameters, the smaller the diameter, the greater the turning angle of the welding gun, leading to a larger circumferential curvature of the small-diameter steel tube and more pronounced geometric undulations on its surface.

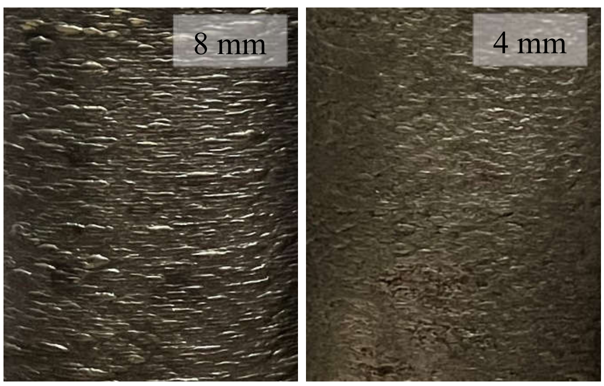

Figure 13. Typical surface profiles of WAAM steel sheets with a thickness of 8 mm and 4 mm

In conclusion, the geometric undulation on the surface of the WAAM steel tubes is influenced by three factors: the statistical dispersion of the cross-sectional areas of the steel tube, the thickness of the printed layer of the steel tube and the diameter of the steel tube. To facilitate the qualitative evaluation of the geometric undulations on the surface of steel tubes, the surface undulation factor ζ_{su} of the WAAM steel tube is introduced, as expressed in Eq. (2).

$$\zeta_{\text{su}} = \frac{A_{\text{sd}}}{D} T_{\text{y}} \tag{2}$$

$$A_{\text{sd}} = \frac{\sum_{1}^{n} \left(A_i - A \right)^2}{n} \tag{3}$$

Where A_{sd} is a discrete coefficient of the cross-sectional areas of the WAAM steel tube; T_{y} is the thickness of the printed layer of the WAAM steel tube; A_i is the cross-sectional area of each contour spacing for the WAAM steel tube; n is the number of contour spacing. As a result, the surface undulation factor of the WAAM steel tubes was calculated using Eqs. (2) and (3), and the values are presented in Table 4.

3. Material Test

3.1. Tensile Test

The material properties of the WAAM steel coupons and their overall stress-strain response were determined following the guidelines of GB/T 228.1-2010 [70]. Tensile coupons were extracted from the WAAM ovals at three different angles (0°, 45°, and 90°) with respect to the deposition direction, as shown in Fig. 2, to assess material anisotropy. Two sets of coupons, with nominal thicknesses of 4 mm and 8 mm respectively, were tested. The study aimed to analyse the impact of geometric undulations on material properties, comparing the response of as-built and machined coupons. In total, 24 tensile tests were carried out to achieve this objective. Fig. 16 illustrates the use of an extensometer and a digital image correlation (DIC) system [37] to obtain precise surface strain measurements for both the machined and as-built coupons. To ensure comprehensive strain calculation across the entire parallel length, white paint was applied to all coupons, followed by a random black speckle pattern before testing. The tensile test was conducted using a 250 kN INSTRON testing machine, operating under displacement control at a rate of 0.8 mm/min. Load and extensometer measurements were recorded at a frequency of

5 Hz, while the DIC system captured the tensile force through two analogue-to-digital converters, acquiring images at the same frequency of 5 Hz.

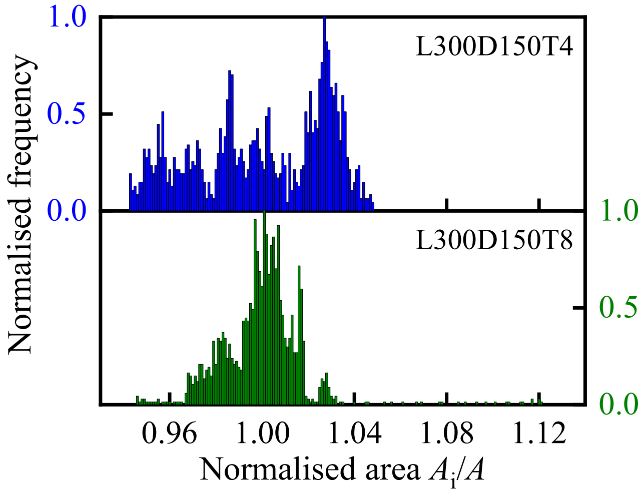

(a) L300D150 series

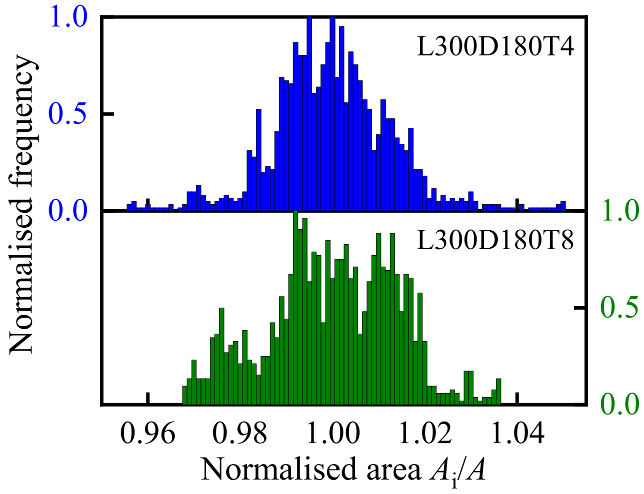

(b) L300D180 series

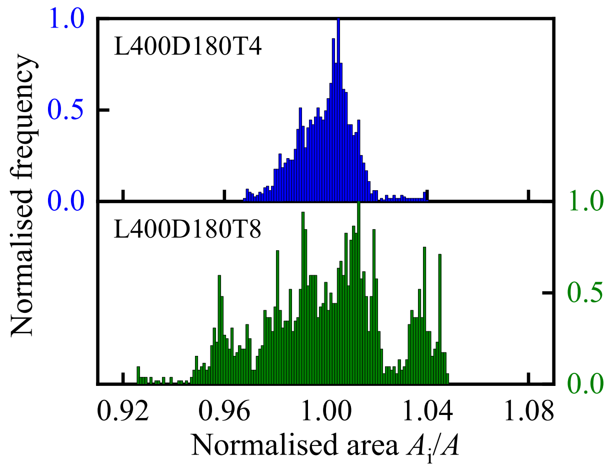

(c) L400D210 series

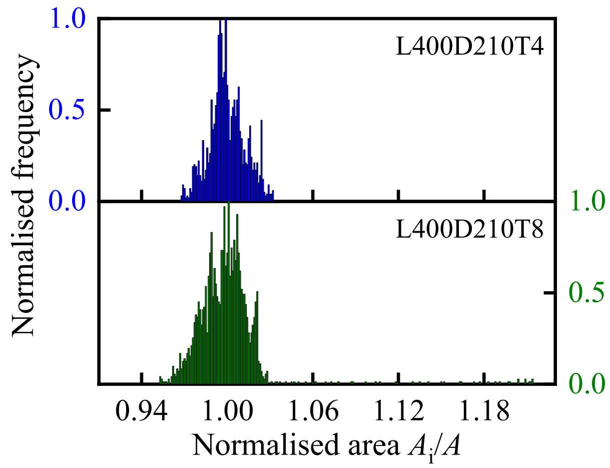

(d) L400D210 series

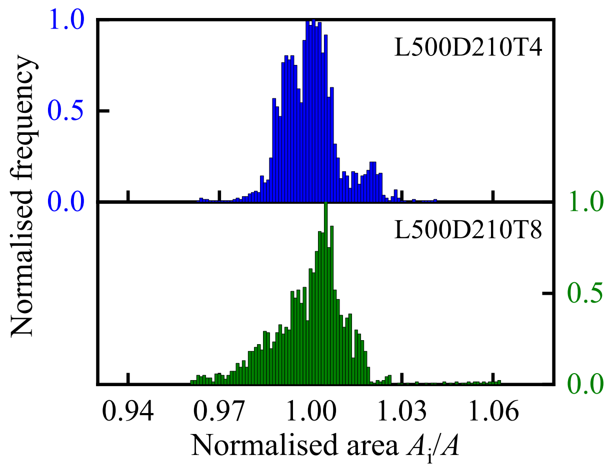

(e) L500D210 series

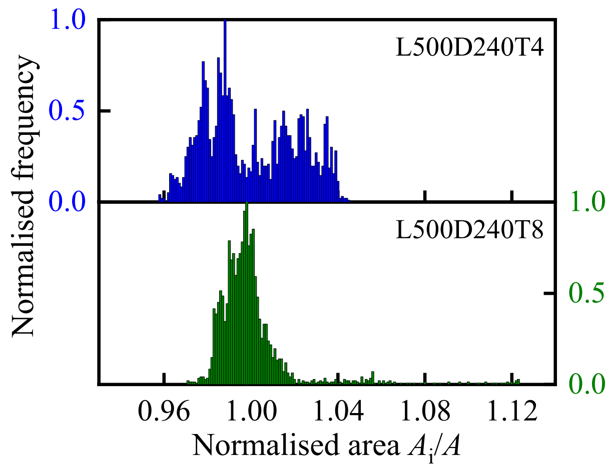

(f) L500D240 series

Figure 14. Variation of the cross-sectional area within WAAM steel tubes

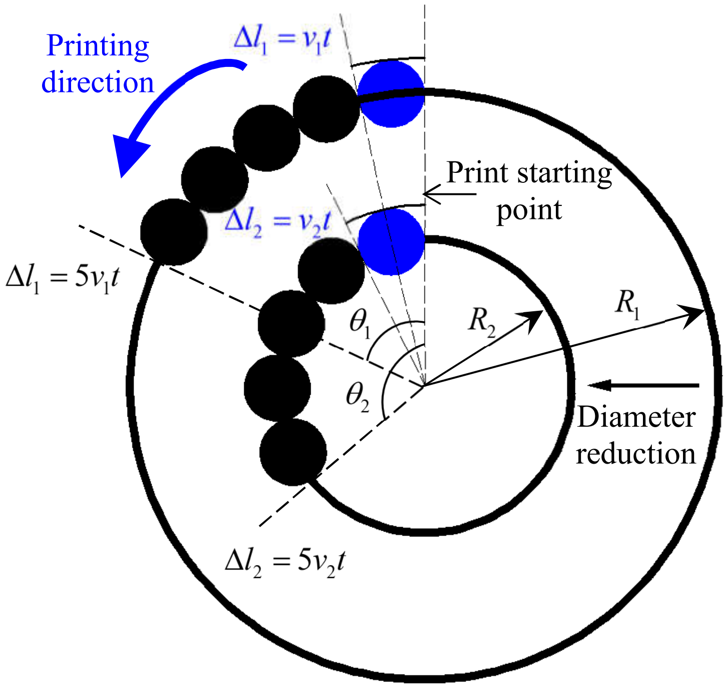

Figure 15. Schematic diagram of undulation degree related to the diameter of WAAM steel tube

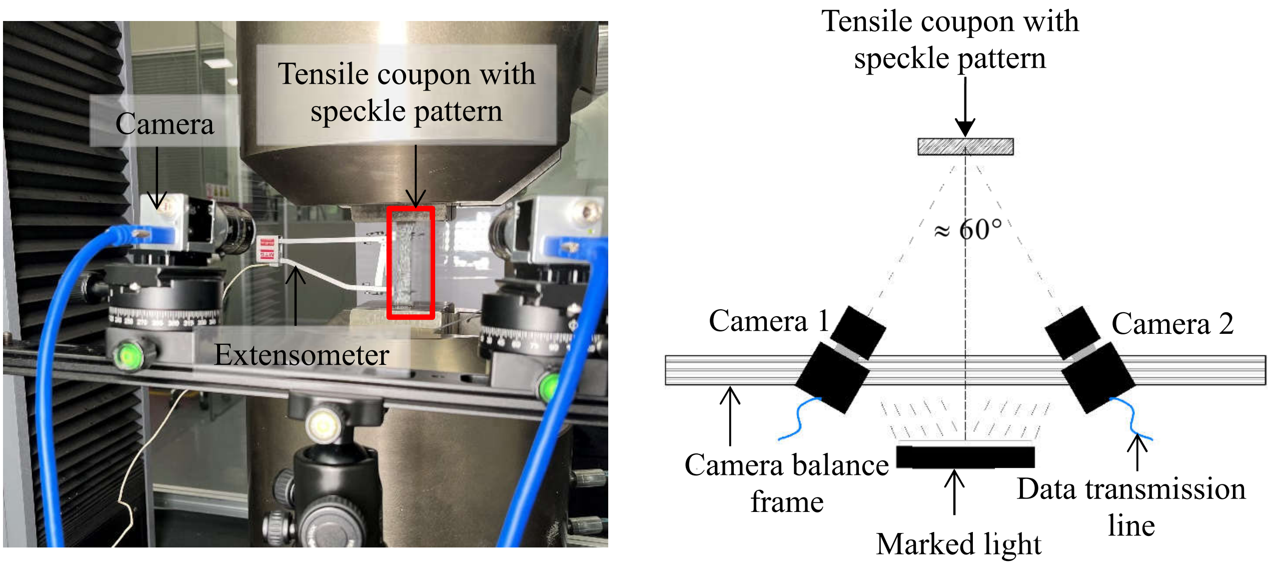

(a) Tensile test setup (b) Plan view of DIC setup

Figure 16. Coupon setup of tensile test and DIC

Fig. 17 shows the fractured coupons, while Fig. 18 shows their respective longitudinal strain plots at the point of fracture, providing a typical example. It was observed that the longitudinal surface strain pattern of as-built coupons was significantly influenced by their inherent anisotropy (namely, coupons exhibit non-uniform distributions of longitudinal surface strain). Despite efforts to remove surface undulations and create prismatic coupons of similar geometry, the machined coupon surfaces still exhibited deformations during testing that aligned with their building direction. This behaviour can be attributed to the anisotropy originating from the preferential crystallographic alignment along the highest thermal gradient, which occurs during the rapid solidification of the melted material [37,38]. As a result, the material behaviour was highly dependent on the direction of loading.

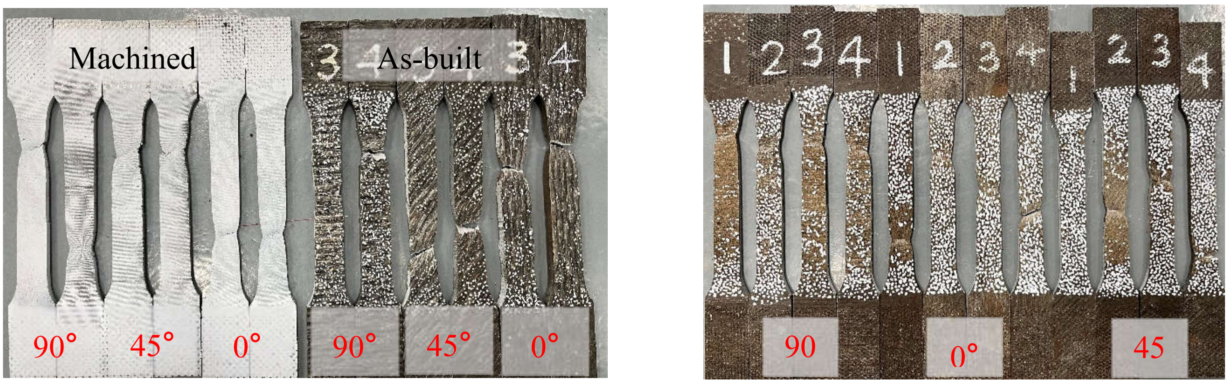

(a) 8 mm tensile coupons (b) 4 mm tensile coupons

Figure 17. Close-up views of coupons after testing

WAAM material displays heterogeneity due to its non-uniform distributions of properties, as depicted in Fig. 18. However, in this study, the constitutive response of WAAM material was investigated by focusing on its average macroscopic properties. Therefore, the mechanical properties were assumed uniformly distributed within the specimens. Figs. 19 and 20 present the engineering stress-strain and stress vs. the Poisson's ratio curves, respectively. Positive strain values indicated material elongation, while negative values indicated material contraction. Additionally, a linear regression analysis (LRA) method was employed to calculate the elastic modulus E_s. A summary of the average material properties of the as-built and machined steel coupons, grouped by deposition direction (i.e., 0°, 45° and 90°) is reported in Table 5; where E_s is the elastic modulus, f_y is the yield strength, f_u is the ultimate strength, and ε_u is the fracture strains. In general, the mechanical properties of the as-built coupons were observed to be slightly inferior to those of the machined coupons. This finding highlights the negative impact of the surface undulations resulting from the Wire Arc Additive Manufacturing (WAAM), as these properties are highly sensitive to the loading direction in relation to the deposition direction. Additionally, some degree of mild anisotropy was noted, with thinner coupons exhibiting a more pronounced anisotropic behaviour. Moreover, the Poisson's ratio μ_s of the coupons generally fell within the range of 0.2 to 0.45. Notably, during the elastic-plastic stage, the Poisson's ratio of most coupons remained stable at approximately 0.35.

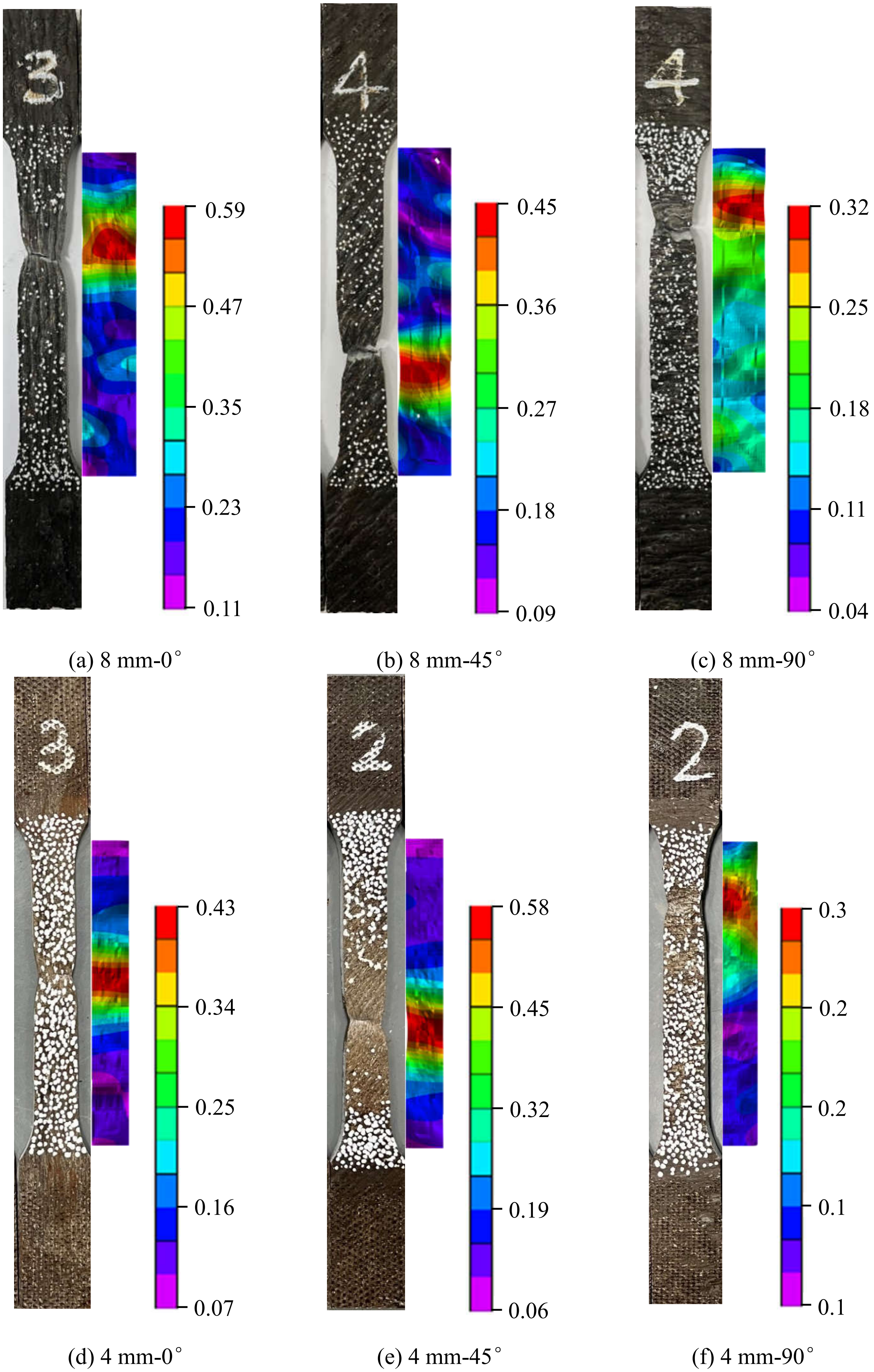

Figure 18. Typical longitudinal strain fields of coupons before coupons fracture

Table 5 Average material properties of WAAM steel coupons

θ	t_n (mm)	E_s (GPa)	f_y (MPa)	f_u (MPa)	ε_u	Note
90°	8	190.10	324.77	446.97	0.19	As-built
		194.94	364.38	483.45	0.18	Machined
	4	184.05	433.53	535.98	0.15	As-built
45°	8	200.58	339.92	460.55	0.16	As-built
		208.73	357.20	471.51	0.15	Machined
	4	210.10	442.98	511.56	0.15	As-built
0°	8	191.62	355.69	464.86	0.17	As-built
		196.90	368.38	482.06	0.21	Machined
	4	199.40	444.28	535.98	0.15	As-built

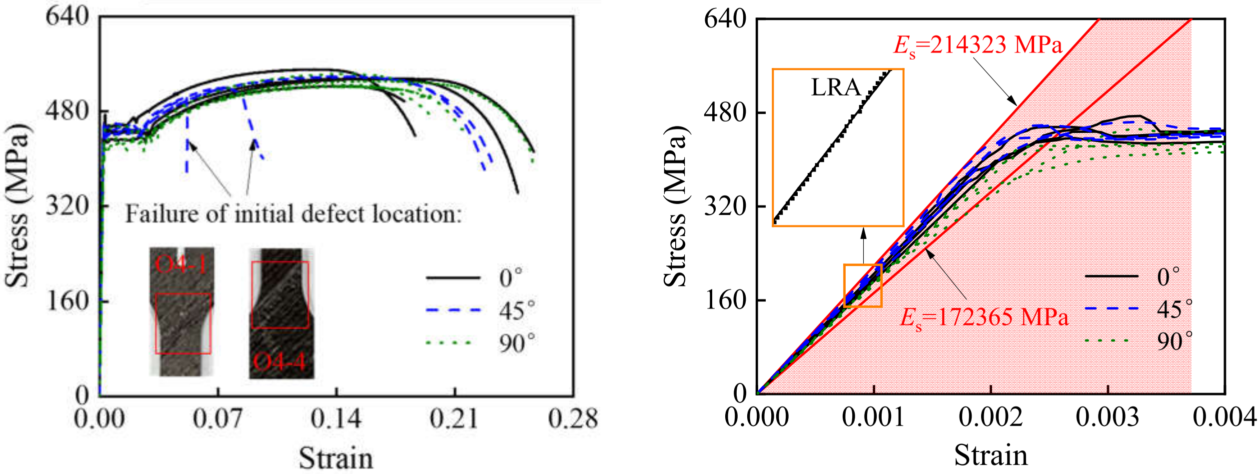

(a) 4 mm thick coupon

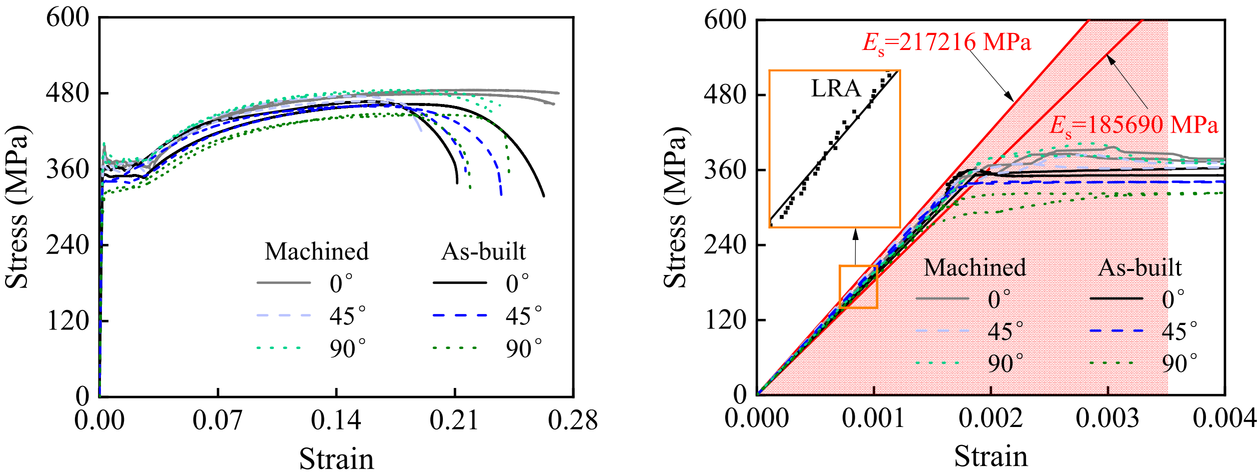

(b) 8 mm thick coupons

Figure 19. Stress-strain curves obtained from tensile coupon tests: full curve (left), initial range (right)

3.2. Concrete Cubic Tests

To determine the material properties of the inner concrete, three concrete cubes were tested. The compressive strength of the concrete cubes was determined at the age of 28 days [71] by testing them at a constant displacement rate of 0.25 mm/min. The mean compressive strength of the concrete cubes was measured as f_{cu}=37.43 MPa. The compressive strength of the inner concrete was taken as f_c=0.8f_{cu}=29.94 MPa, and the elastic modulus was taken as $E_c = 4730\sqrt{f_c}$=25881.36 MPa .

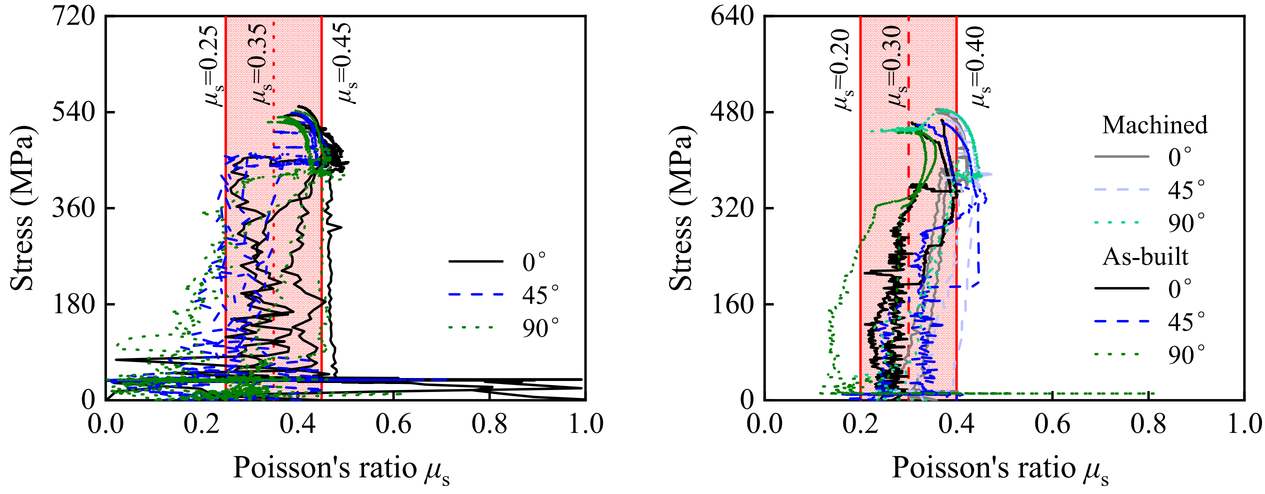

(a) 4 mm thick coupons

(b) 8 mm thick coupons

Figure 20. Poisson’s ratio obtained from tensile coupon tests: average value of DIC

4. Push-out Tests

4.1. Specimen Design and Preparation

A total of twelve concrete-filled WAAM steel tube specimens were designed and tested, while the main test parameters included: 1) diameter to thickness ratio of WAAM steel tube (*D*/*T*); 2) length to diameter ratio of WAAM steel tube (L_e/*D*). The geometric dimensions of the WAAM steel tube determined by Rhino [68] based on the scanned 3D models were used for the CFST specimens, as shown in Table 6, in which the labels of CFST specimens were defined by the order of member type and the dimensions of WAAM steel tube, and L_e is the interface length of the tube to the concrete. The label "CF" refers to a concrete filled WAAM steel tube. The other labels are defined similarly to those in the WAAM steel tube, as mentioned in Section 2.1.

After the concrete was mixed, it was poured into the WAAM steel tubes and compacted using a poker vibrator. To allow for slip between the concrete and the tube during the testing arrangement, the WAAM steel tubes were filled to a length 45 mm longer than the height of the inner concrete. Following 28 days of standard curing, the length difference between the steel tube and inner concrete was measured to account for the shrinkage effect of the latter.

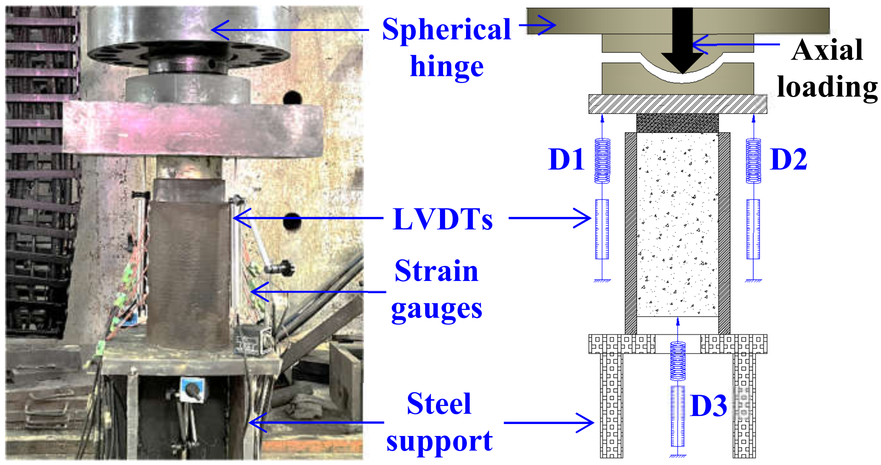

Figure 21. Test setup of axial compressive tests on push-out CFST specimens

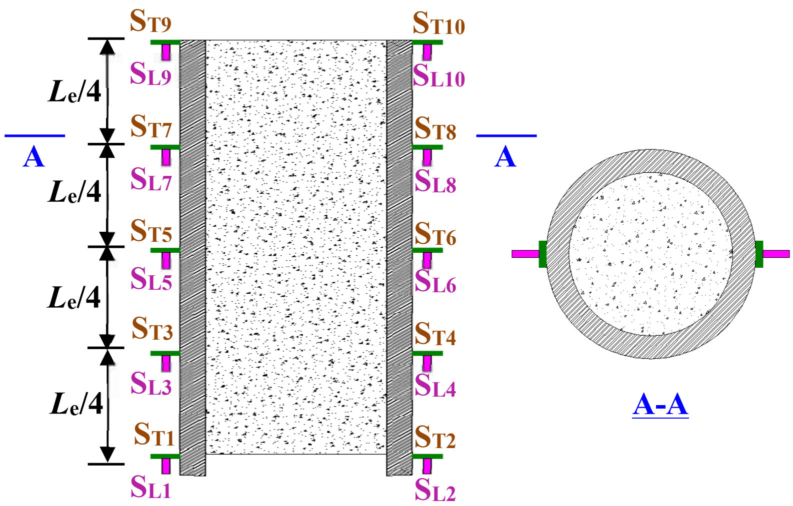

Figure 22. Arrangement of strain gauges on push-out CFST specimens

4.2. Test Setup and Instrumentation

The experimental layout adopted for the conducted tests is shown in Fig. 21. A 10,000 kN electric-hydraulic jack was used for the application of the axial load, tested at displacement rates of 0.25 mm/min for pre-peak stage and 0.5 mm/min for post-peak stage [72,73], respectively. A steel cylinder block was placed on the top of the push-out specimen to transfer the load, where the outer diameter of the block was slightly smaller than that of the inner concrete. Spherical hinge supports were employed at the steel cylinder block to ensure that the axial force was evenly transferred between the CFST specimens and the loading plates. The inner concrete was then pushed out together during testing. Note that the geometric centroids of the ends for the specimens were aligned with the centroid of the loading plate to avoid eccentric loading as much as possible.

Two LVDTs (D1-D2) were symmetrically positioned at the specimen loading end to measure vertical displacements, while one LVDT (D3) was installed at the free end of the specimen, as shown in Fig. 21. Ten transverse and ten longitudinal strain gauges (S_{T1}~ S_{T10} and S_{L1}~ S_{L10}) were attached uniformly to the CFST specimens - see Fig. 22, to measure the horizontal and vertical strains. The strain gauges spaced at 60 mm, 85 mm and 110 mm intervals were installed along the length of the steel tube for specimens with a length of 300 mm, 400 mm and 500 mm, respectively. Prior to attaching the strain gauges, the surface of the WAAM steel tube shall be slightly polished to provide a smooth surface for the attachments. During the testing, the load was stopped when the displacement of the load cell reached 30 mm for L300 and L400 series and 40 mm for L500 series, respectively. The load cell, LVDTs and strain gauges reading were taken at a frequency of 1 HZ.

4.3. Results and Discussions

4.3.1. Experimental Observations

Figs. 23 presents the failure modes of specimens, while local observations on the interface are also presented in Figs. 23(b)-(d), along with the general failure mode of the tested specimens. As shown in the figures, the inner concrete moved along the WAAM steel tube, while some of the concrete on the contact surface fell off at the loading end.

After the push-out test, scratches were observed on the interfacial surfaces of the WAAM steel tube and inner concrete. Meanwhile, some concrete debris was found at the contact surface of the tube, as the shear failure layer was formed, and more concrete remained on the thicker steel tube, as shown in Figs. 23(b)-(c). This is due to the fact that the surface of the WAAM steel tube was rougher for the thicker tube wall. In addition, at the free end, specimens had slippage at the interface, and the integrity of the inner concrete was maintained as shown in Fig. 23(b). Furthermore, it can also be observed that except for the CF-L500D240T4 specimen, no obvious deformation or bulking was found in the WAAM steel tube. Local buckling, which occurred at the bottom of the steel tube near the air gap, can be observed in the CF-L500D240T4 specimen, as shown in Fig. 23 (d). This is owing to the high push-out force transferred from the inner concrete to the WAAM steel tube and the local tube wall being too thin with geometric undulations.

(a) Loading and free ends of the specimens before and after the test

(b) Typical interfacial surfaces of tube and concrete after push-out test

(c) Comparison of loading ends with different tube thickness

(d) Local buckling of CF-L500D240T4 specimen

Figure 23. Failure modes of the push-out specimens

4.3.2. Load-Slip Relationship and Bond Strength

The load versus slip curves of the push-out specimens are plotted in Fig. 24, in which the slip value of the loading end was calculated by the average readings of D1 and D2, and the slip value of the free end was measured by D3. It can be found that the load increased linearly and rapidly with the slip displacement in the initial stage of loading. In the initial stage, the interfacial bond behaviour of the WAAM steel tube and concrete was mainly composed of chemical adhesion and interlocking, where the chemical adhesion is formed by intermolecular forces between the cement gel and the steel tube, and the interlocking force is the mechanical interaction between the tube and concrete caused by the geometric undulations of WAAM steel tube. After reaching the peak load, a slowly descending region appeared until a relatively stable residual load was achieved, which could be explained by the fact that the broken concrete filled the undulations surface of the WAAM steel tube leading to the reductions of chemical adhesion and minor reduction of the interlocking force and hence the bond strength. It is somewhat different from the research results of the push-out specimens fabricated by conventional steel tubes [22,24-26,28,29,31] where a rapidly declining region can be found caused by the disappearance of chemical adhesion and significant reduction of the micro-interlocking force in this stage. This is attributed to the fact that conventional steel tubes, such as stainless steel and low-carbon steel, have a relatively smooth surface whilst the WAAM steel tubes exhibiting an undulated surface.

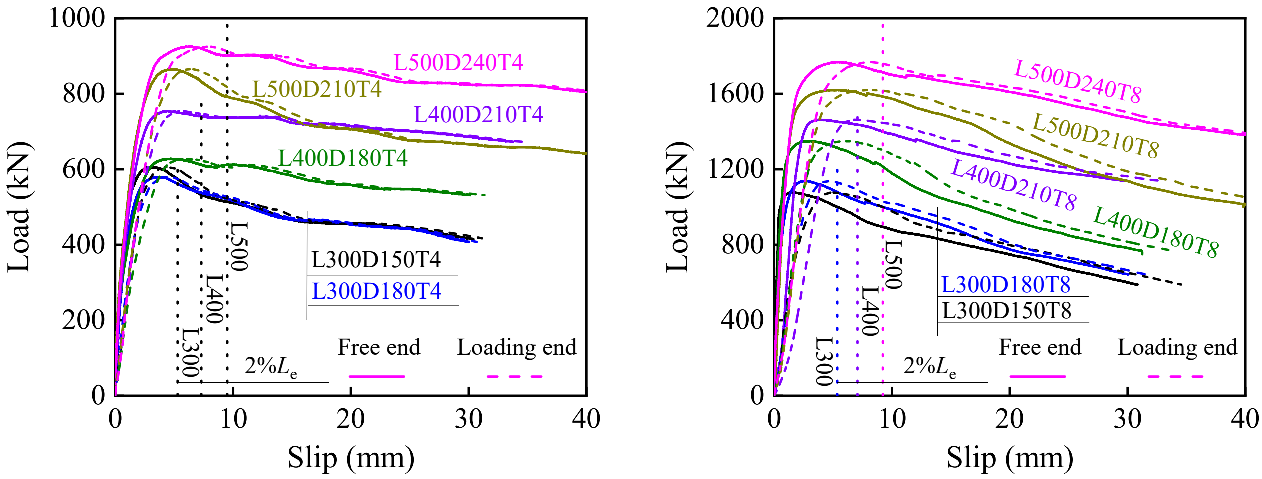

(a) Specimens with 4 mm thick wall (b) Specimens with 8 mm thick wall

Figure 24. Load-slip curves of push-out CFST specimens

In addition, it can also be seen from Fig. 24 that when reaching the same load level, the slip displacement of the loading end was greater than that of the free end, and the larger the thickness of the WAAM steel tube, the greater the difference between the slip displacements of the loading and free ends. Similarly, for the specimens with identical nominal diameter and length, the larger the thickness of the WAAM steel tube, the smaller the slip displacements of the free end when reaching the peak load, as shown in Fig. 25. These reveal that the thicker the WAAM steel tube, the increase in compressive deformation of inner concrete itself and the decrease in the slip displacements of free end led to an increase in the compressive load. This is due to the fact that the factor of surface undulation for the WAAM steel tube is positively correlated with the tube wall thickness, as described in Section 2.3. It should be noted that the slip at the peak load for all push-out specimens in this paper meets the requirement that the allowable slippage is usually kept to less than 2% of the effective contact length L_e to ensure the applicability of real structures [22,28,29,31], as shown in Fig. 25. The slip displacement of the free end was used as the slip amount of the inner concrete.

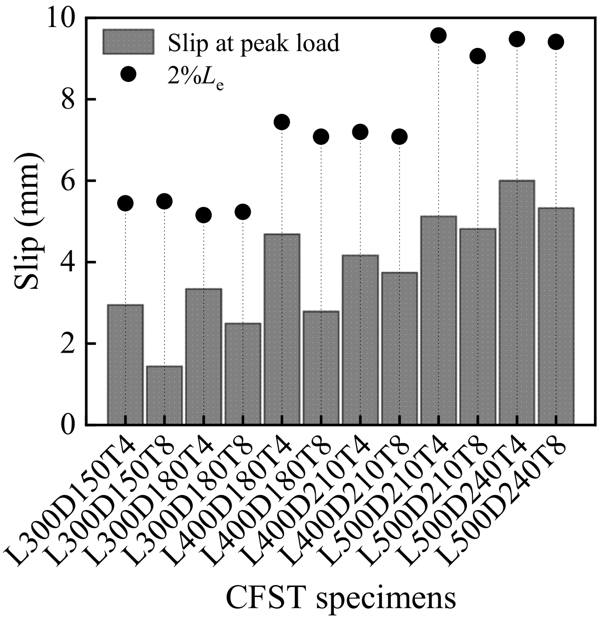

Figure 25. Slip of push-out CFST specimens

The average and residual bond stresses were adopted to quantify the interface bond behaviour, which was defined by dividing the push-out load by the contact area of the inner interface. Assuming that the bonding stress is evenly distributed on the contact area, the interfacial average and residual bond strengths (τ_u and $\tau_{u\_2\%}$) in concrete-filled WAAM steel tubes can be defined as Eqs. (4) and (5):

$$\tau_u = \frac{N_u}{\pi D L_e} \quad (4)$$

$$\tau_{u\_2\%} = \frac{N_{u\_2\%}}{\pi D L_e} \quad (5)$$

where N_u is the peak load of the push-out specimens, $N_{u\_2\%}$ is the residual load when the slip reaches 2% of the interface length L_e at the post-peak segment [22,28,29,31]. The average τ_u and residual $\tau_{u\_2\%}$ bond stresses are summarised in Table 6, where S_u is the slip at the free end when reaching the peak load; $\sigma_s = N_u / A_s$ is the axial stress of the WAAM steel tube within the air gap; A_s is the average cross-sectional area of the WAAM steel tube. It can be found that the axial stresses of the WAAM steel tubes within the air gap were less than their corresponding yield strengths, indicating that the WAAM steel tubes of the push-out specimens were not failed under compression. The average bond stresses of the push-out specimens were far greater than those of the push-out specimens fabricated by conventional steel tubes [22,24-26,28,29,31] and even checkered steel tubes [23]. This is because the roughness caused by the surface undulations of WAAM steel tubes is more significant than conventional and checkered steel tubes, which can improve the bond strengths of the CFST specimens with WAAM elements. In addition, the average ratio of the residual and average bond stress was 0.96, with CoV of 0.024, demonstrating only a minor reduction of the interlocking force between the WAAM steel tube and inner concrete until the attainment of the 2%L_e slip.

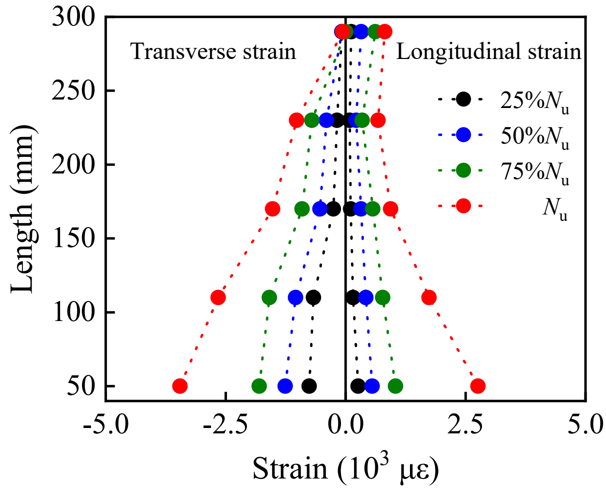

(a) L300D150T4

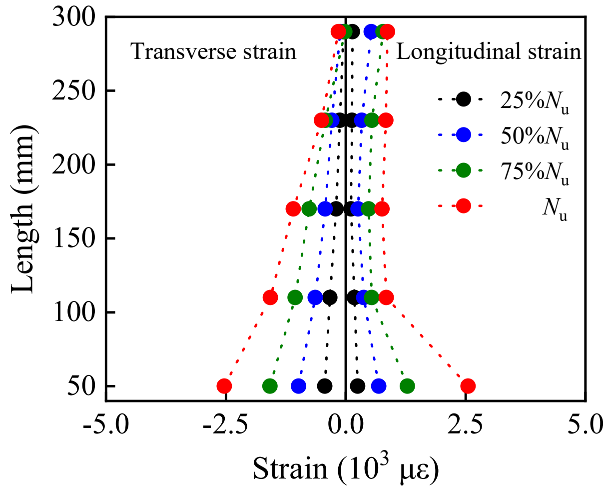

(b) L300D180T4

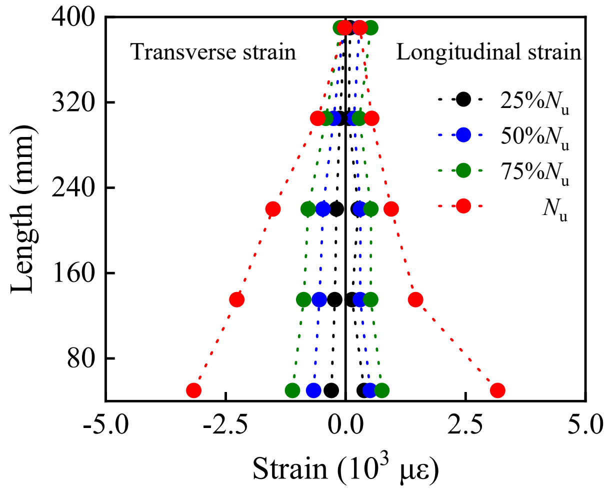

(c) L400D180T8

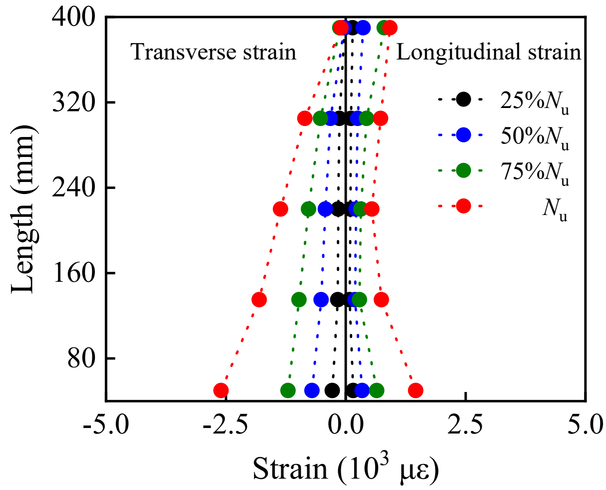

(d) L400D210T4

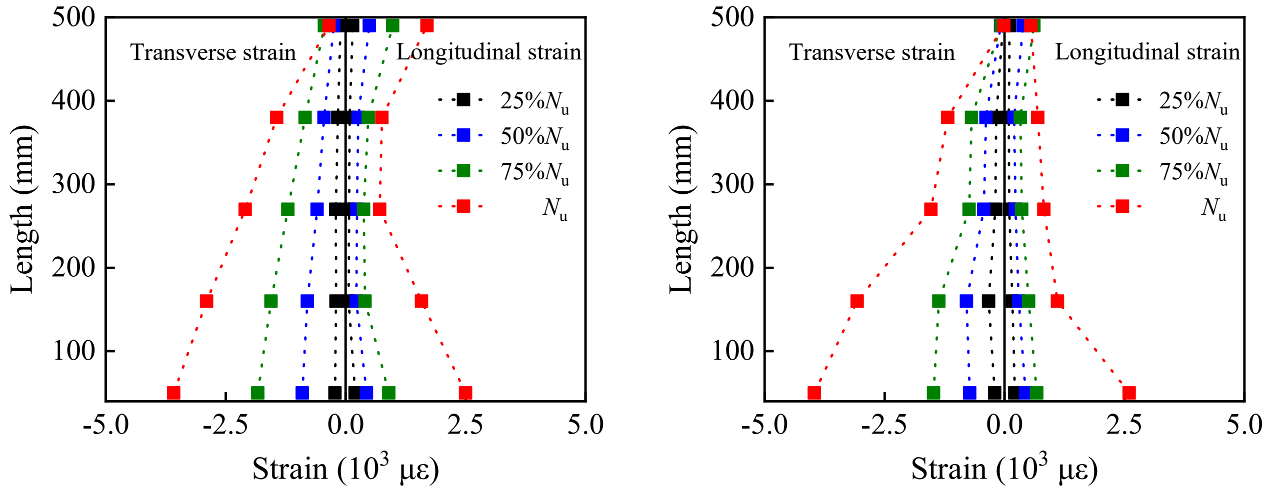

(e) L500D210T4 (f) L500D210T8

Figure 26. Strain distribution of the WAAM steel tube of specimens

4.3.3. Strain and Stress Distribution of WAAM Steel Tube

The longitudinal and transverse strain distributions of the WAAM steel tubes for the push-out specimens at four loading stages, namely 25%, 50%, 75% and 100% of the peak load, are illustrated in Fig. 26. The vertical axis is the length of the tube wall from the free end to loading end along the longitudinal direction. In these plots, positive strain values indicate material contraction, while negative values indicate material elongation. It can be seen that the longitudinal strain values of the WAAM steel tube increased with an increase in the compressive load, while the longitudinal strain values at the free end of the specimen were larger than those at the loading end, basically. This indicates the shear load was transferred to the tube from the concrete through accumulative bond stress. The negative transverse strain values indicate that the confinement was provided by the WAAM steel tube to the inner concrete. The transverse strains increase along the height direction from loading end to free end of the specimens is attributed to the shear load being transferred to the tube along the height and compressive expansion of the inner concrete near the free end. Some of the strain values did not conform to the above distribution, this might be due to local buckling caused by geometric undulations on the surface of the WAAM steel tube.

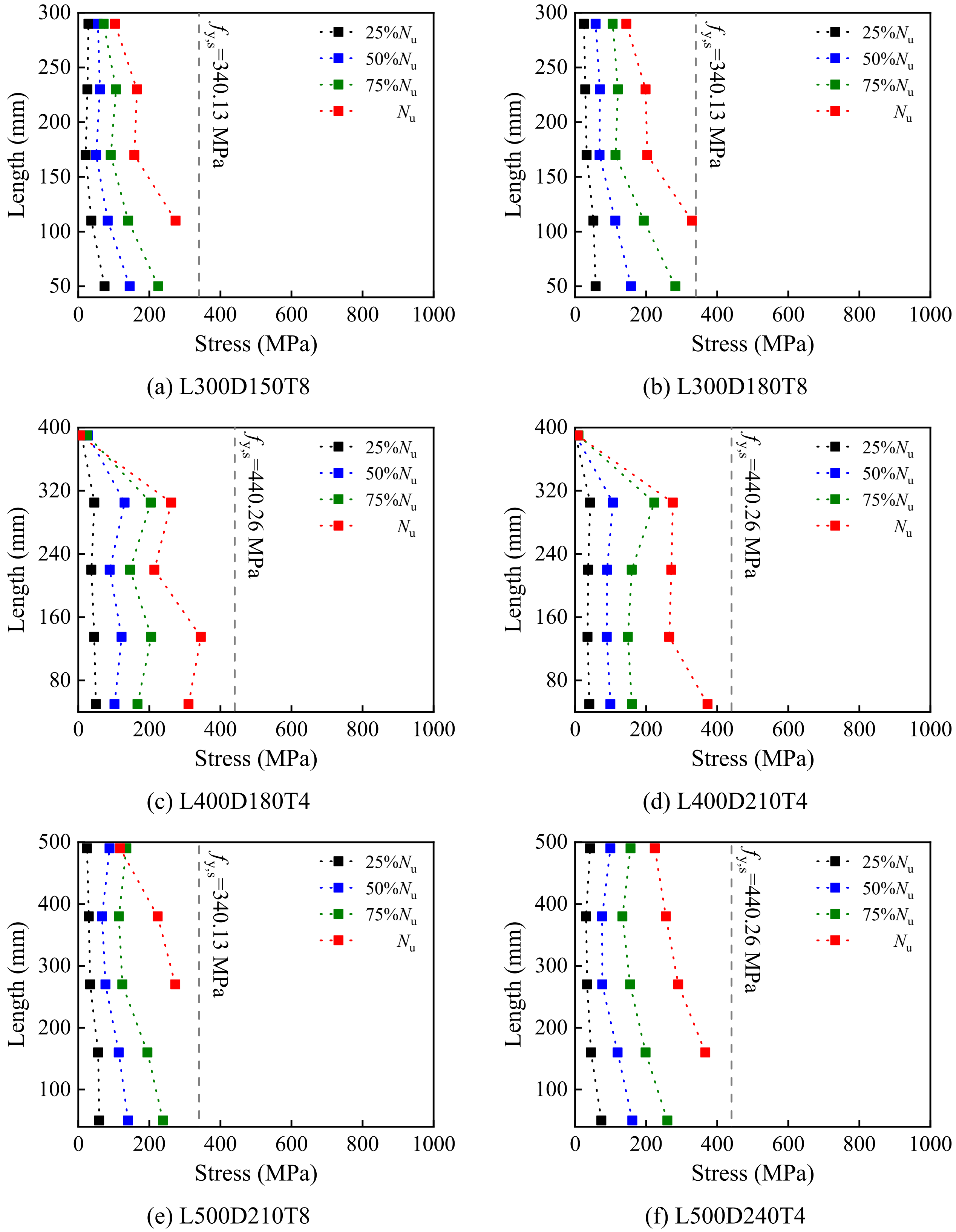

Figure 27. Stress distribution of the WAAM steel tube of specimens

The calculated stresses of the WAAM steel tubes (see Table 6) indicate that the steel tubes of all specimens generally remained elastic during the push-out test except for local buckling at the bottom of the steel tube near the air gap. Therefore, the influence of yield stress on the bond behaviour can be ignored. Based on the longitudinal and transverse strains measured along the length of a specimen and the assumption that the steel tube remained in the elastic stage during the whole loading process, the longitudinal stress σ_L of WAAM steel can be derived according to Eq. (6) [20,24,29]:

$$\sigma_L = \frac{E_s}{1-\mu_s^2}\left(\varepsilon_L + \mu\varepsilon_\theta\right) \tag{6}$$

where ε_L and ε_θ are the longitudinal and transverse strains of the WAAM steel tube, respectively. The longitudinal stress distributions of specimens are shown in Fig. 27. As predicted, the longitudinal stress generally increases from the loading end to the free end due to the shear load being transferred from the inner concrete to the WAAM steel tube. The calculated stress at some strain gauge positions, which are greater than the material yield stress, are not shown in Fig. 27, because local buckling occurred at these strain gauge locations which is not conform to the assumption of elastic state. It should be noted that at the height of these strain gauges, the full cross-section of the WAAM steel tube was not all reached yield stress state, as evidenced by the average stresses of the WAAM steel tubes in Table 6.

4.3.4. Influence of Different Parameters of the WAAM Steel Tube

(1) Geometric undulations

Steel tubes with different surface geometric undulations ζ_{su} were used to study the effects of surface roughness on bond strength. Fig. 28(a) shows the influence of surface geometric undulation on the bond strength τ_u. As predicted, a significant positive correlation between bond strength and the factor of the geometric undulation can be found in Fig. 28(a), indicating that the bond strength was greater when the geometric undulation of the WAAM steel tube was larger. This is due to the fact that the friction effect can be improved by the geometric undulation, resulting in the enhanced interfacial bond strength.

(2) Diameter to thickness ratio

The diameter-to-thickness ratio of the WAAM steel tube (*D*/*T*) significantly influences the interfacial bond strength in CFST members with conventional steel tubes [22,24,28,28,31]. In this paper, the *D*/*T* still had a significantly effect on the average bond strength for the concrete-filled WAAM steel tube specimens, as shown in Fig. 28(b). Like the CFST members with conventional steel tubes, the average bond strength of specimens generally decreased with an increase of *D*/*T*. This is attributed to the decrease of the confinement effect provided by the WAAM steel tube to inner concrete as D/T increased and hence the bond strength.

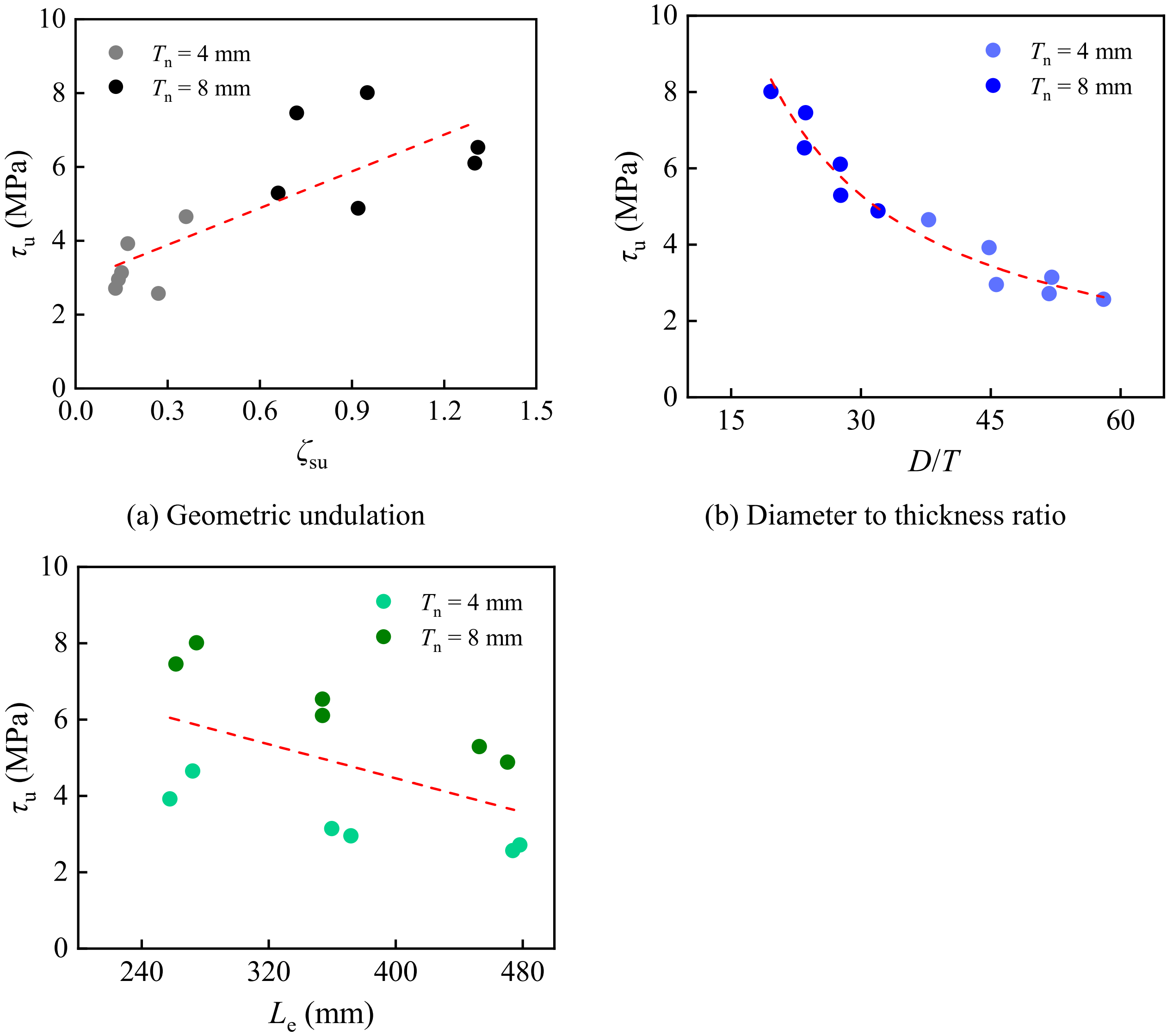

(a) Geometric undulation

(b) Diameter to thickness ratio

(c) Interface length

Figure 28. Influence of different parameters on the interfacial bond stress

(3) The interface length

The trend of the average bond strengths of specimens with different effective lengths (L_e) is shown in Fig. 28(c). It can be found that the increase of L_e led to a moderate decrease in the average bond strength, which was consistent with the results of push-out specimens with conventional steel tubes [29,31].

This might be due to the uneven distribution of bonding stress on the contact area, while the contact area was determined in terms of the effective length, therefore the average bond strength decreased with longer interfacial effective length.

Table 6 Comparisons of design predictions and experimental results of CFST specimens

Specimens ID	ζ_{su}	L_e (mm)	S_u (mm)	N_u (kN)	σ_s (MPa)	τ_u (MPa)	$\tau_{u\_2\%}$ (MPa)	$\frac{\tau_{u\_2\%}}{\tau_u}$	AISC 360-16 $\frac{\tau_{u,AISC}}{\tau_{u,Exp}}$	EC4 $\frac{\tau_{u,EC4}}{\tau_{u,Exp}}$	AS 5100 $\frac{\tau_{u,AS}}{\tau_{u,Exp}}$	AIJ $\frac{\tau_{u,AIJ}}{\tau_{u,Exp}}$	Proposed design $\frac{\tau_{u,Design}}{\tau_{u,Exp}}$
CF-L300D150T4	0.36	272.2	2.95	606	322.56	4.65	4.38	0.94	0.20	0.12	0.09	0.05	0.95
CF-L300D150T8	0.95	274.5	1.44	1077	291.40	8.01	7.42	0.93	0.17	0.07	0.05	0.03	1.10
CF-L300D180T4	0.17	257.8	3.34	579	253.98	3.92	3.82	0.97	0.17	0.14	0.10	0.06	0.95
CF-L300D180T8	0.72	261.6	2.49	1138	259.16	7.46	7.10	0.95	0.16	0.07	0.05	0.03	0.98
CF-L400D180T4	0.14	371.9	4.69	628	281.21	2.95	2.87	0.97	0.22	0.19	0.14	0.08	1.15
CF-L400D180T8	1.31	353.9	2.79	1349	305.28	6.53	6.15	0.94	0.19	0.08	0.06	0.03	1.06
CF-L400D210T4	0.15	359.8	4.17	754	282.39	3.14	3.09	0.98	0.15	0.18	0.13	0.07	0.95
CF-L400D210T8	1.30	353.9	3.74	1462	287.35	6.10	6.00	0.98	0.15	0.09	0.07	0.04	0.96
CF-L500D210T4	0.13	478.3	5.12	865	322.82	2.71	2.48	0.92	0.18	0.20	0.15	0.08	1.02
CF-L500D210T8	0.66	452.8	4.82	1620	319.41	5.29	5.18	0.98	0.17	0.10	0.08	0.04	1.04
CF-L500D240T4	0.27	473.8	6	925	296.90	2.57	2.50	0.97	0.15	0.21	0.16	0.09	0.96
CF-L500D240T8	0.92	470.5	5.33	1768	309.66	4.88	4.72	0.97	0.14	0.11	0.08	0.05	0.95
							Mean	0.96	0.17	0.13	0.10	0.05	1.00
							CoV	0.024	0.135	0.395	0.395	0.395	0.069

5. The Interfacial Bond Strength of Concrete-filled WAAM Steel Tube

In this section, the average bond strengths of the push-out specimens were also initially compared against the bond strength predictions of the CFST member comprising of conventional steel tube (such as carbon steel or stainless steel) by current design codes, namely AISC 360-16 [46], EC4 [65], AS 5100 [66]and AIJ [67]. In addition, the design equation of the average bond strength of concrete-filled WAAM steel tubes was proposed, while the geometric undulations of the WAAM steel tubes (as aforementioned in Section 2.3) were considered. The applicability of the proposed equation was subsequently evaluated.

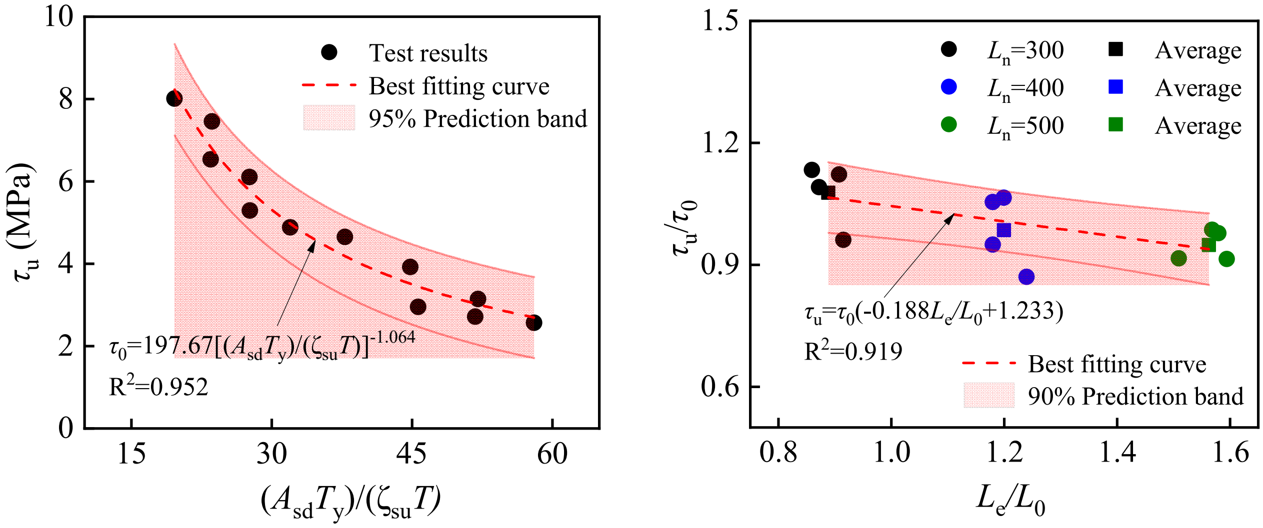

(a) Influences of ζ_{su} and D/T (b) Influence of L_e

Figure 29. Predictions of the average bond strengths

5.1. Current Design Codes

The specified design bond strength in AISC 360-16 [46] are expressed in Eq. (7), while the design bond strengths in EC4 [65], AS 5100 [66] and AIJ [67] are 0.55 MPa, 0.4 MPa and 0.225 MPa for the circular CFST members, respectively. Since the specified bond strengths were proposed based on CFST members with conventional steel tubes, there is a need to check the validity of the specifications, especially to consider the effect of surface roughness on the bond strength.

$$\tau_{u,AISC} = 5300\frac{T}{D^2} \leq 1.4 \quad (7)$$

Comparisons of design predictions and experimental results of push-out specimens are summarised in Table 6. The results show that the predictions in standards of AISC 360-16, EC4, AS5100 and AIJ were overly conservative compared to the experimental bond strength of the specimens, namely, the maximum predicted value from these codes is less than 25% of the corresponding experimental value. This highlights that special attention should be paid when using the specified design bond strengths in the current standard to design the CFST member comprising WAAM steel tubes. The bond strength of the concrete-filled WAAM steel tube is enhanced by the geometric undulation of the surface, and hence the factor of the surface undulation should be taken into account for the prediction of bond strength.

5.2. Proposed Bond Strength

The parameters of the factor of geometric undulation ζ_{su}, the diameter-to-thickness ratio D/T and interface length L_e exhibit a significant influence on the bond strength of the concrete-filled WAAM steel tube. Therefore, the bond strength of the concrete-filled WAAM steel tube could be predicted by using the design equations presented in Eqs. (8) and (9). The relationship of criterion bond strength τ_0 with the parameter of the factor of geometric undulation ζ_{su}, or the diameter-to-thickness ratio D/T is shown in Fig. 28(a), while the best-fitting curve of a power relationship with 95% prediction band is presented in Fig. 29(a). The relationship of normalized bond strength $\tau_{\mathrm{u,Design}} / \tau_0$ with the parameter of the interface length L_e is shown in Fig. 29(b).

$$\tau_0 = 197.67\left(\frac{D}{T}\right)^{-1.064} = 197.67\left(\frac{A_{\mathrm{sd}}T_y}{\zeta_{\mathrm{su}}T}\right)^{-1.064} \tag{8}$$

$$\tau_{\mathrm{u,Design}} = \tau_0(-0.188\frac{L_e}{L_0} + 1.233) \tag{9}$$

where τ_0 is the criterion bond strength of concrete-filled WAAM steel tube without considering the influence of interface length L_e; L_0=300 mm is a reference length. The predictions calculated using the proposed design approach of the concrete-filled WAAM steel tube specimens were compared with the experimental results $\tau_{\mathrm{u,Exp}}$, as shown in Table 6. It can be seen that the predictions calculated by the proposed approach were close to the experimental bond strength of the specimens with the mean value of $\tau_{\mathrm{u,Design}} / \tau_{\mathrm{u,Exp}}$ being 1.00, and the CoV being 0.069. Generally, the proposed design equation can predict the average bond strength of the concrete-filled WAAM steel tubes with reasonable accuracy. It should be noted that the proposed equations are validated within the range of the parametric study, i.e. $15 \leqslant D/T \leqslant 60$ and $300 \leq L \leq 550$. Further research is required for the wider applicability of the design of the concrete-filled WAAM steel tube.

6. Conclusions

In this paper, the geometric characteristics and material properties of the WAAM steel components were intensively examined. Subsequently, the experimental research was carried out to elucidate the interfacial bond behaviour of the concrete-filled WAAM steel tube. A design approach for predicting bond strength was introduced. The summarised findings from this investigation can be outlined as follows:

(1) The comparison results indicate that the 3D laser scanning method was the most suitable approach for achieving precise measurements of WAAM steel element geometry. The factor of surface undulation was proposed to quantitatively evaluate the roughness of the WAAM steel tube.

(2) Material properties of the WAAM steel coupons which were extracted from different deposition direction, were acquired through monotonic tensile tests. Mild anisotropy was evident, with a more notable effect observed in the thinner coupon specimens.

(3) The experimental results demonstrate that: 1) after reaching the peak load, a slowly descending region appears until a relatively stable residual load was achieved, which is somewhat different from the research results of the push-out specimens fabricated by conventional steel tubes; 2) the average bond stresses of the push-out specimens were far greater than that of the push-out specimens fabricated by conventional steel tubes and even checkered steel tubes; 3) the strain values at the free end of the specimen were larger than those at the loading end, indicating the shear load being transferred to the tube from the concrete through accumulative bond stress.

(4) The parameters of the factor of geometric undulation ζ_{su}, the diameter-to-thickness ratio D/T and interface length L_e exhibited a significant influence on the bond strength of the concrete-filled WAAM steel tube.

(5) The predictions of bond strengths in the current codes of AISC 360-16, EC4, AS5100 and AIJ were quite conservative for the specimens with WAAM elements. A design approach for the bond strength of the specimen was proposed. The comparison results demonstrate the proposed design equation could reasonably predict the bond strength of the specimens.

Acknowledgements

The authors would like to thank the financial support from the National Natural Science Foundation of China (NSFC) (Grant Number: 52078249, 52208215), the Natural Science Foundation of Zhejiang Province (Grant Number: LQ22E080008) and the Centre for Balance Architecture of Zhejiang University.

Reference

[1] Ge HB, Usami T. Strength of concrete-filled thin-walled steel box columns: experiment. Journal of Structural Engineering, 1992, 118(11):3036-3054.

[2] Uy B. Strength of short concrete filled high strength steel box columns. Journal of Constructional Steel Research, 2001, 57:113–134.

[3] Han LH, Zhao XL, Yang YF, Feng, JB. Experimental study and calculation of fire resistance of concrete-filled hollow steel columns. Journal of Structural Engineering, 2003, 129(3):346-356.

[4] Sakino K, Nakahara H, Morino S, Nishiyama I. Behavior of centrally loaded concrete-filled steel-tube short columns. Journal of Structural Engineering, 2004, 130(2):180-188.

[5] Zhou F, Young B. Concrete-filled aluminium circular hollow section column tests. Thin-Walled Structures, 2009, 47(11):1272-1280.

[6] Han LH, Chen F, Liao FY, Tao Z, Uy B. Fire performance of concrete filled stainless steel tubular columns. Engineering Structures, 2013, 56:165-181.

[7] Chen J, Ni YY, Jin WL. Column tests of dodecagonal section double skin concrete-filled steel tubes. Thin-Walled Structures, 2015, 88:28-40.

[8] Aslani F, Uy B, Wang ZW, Patel V. Confinement models for high strength short square and rectangular concrete-filled steel tubular columns. Steel and Composite Structures, 2016, 22(5):937-74.

[9] Tao Z, Katwal U, Uy B, Wang WD. Simplified nonlinear simulation of rectangular concrete-filled steel tubular columns. Journal of Structural Engineering, 2021, 147(6):1-19.

[10] Tao Z, Han LH, Wang ZB. Experimental behaviour of stiffened concrete-filled thin-walled hollow steel structural (HSS) stub columns. Journal of Constructional Steel Research, 2005, 61:962-983.

[11] Yu Q, Tao Z, Wu YX. Experimental behaviour of high performance concrete-filled steel tubular columns. Thin-Walled Structures, 2008, 46:362-370.

[12] Liang QQ, Fragomeni S. Nonlinear analysis of circular concrete-filled steel tubular short columns under axial loading. Journal of Constructional Steel Research, 2009, 65(12):2186-2196.

[13] Uy B, Tao Z, Han LH. Behaviour of short and slender concrete-filled stainless steel tubular columns. Journal of Constructional Steel Research, 2011, 67(3):360-378.

[14] Aslani F, Uy B, Tao Z, Mashiri F. Behaviour and design of composite columns incorporating compact high-strength steel plates. Journal of Constructional Steel Research, 2015, 107:94-110.

[15] Xiong MX, Xiong DX, Liew JYR. Axial performance of short concrete filled steel tubes with high- and ultra-high-strength materials. Engineering Structures, 2017, 136:494-510.

[16] Hou C, Zhou XG. Strength prediction of circular CFST columns through advanced machine learning methods. Journal of Building Engineering, 2022, 15:104289.

[17] Zhang YZ, Xu Q, Wang QH, Zhou M, Liu HQ, Guo HY. Axial compressive behavior of circular concrete-filled steel tube stub columns prepared with spontaneous-combustion coal gangue aggregate. Journal of Building Engineering, 2022, 48:103987.

[18] Chen WG, Xu JJ, Li ZP, Huang XL, Wu YT. Load-carrying capacity of circular recycled aggregate concrete-filled steel tubular stub columns under axial compression: Reliability analysis and design factor calibration. Journal of Building Engineering, 2023, 66:105935.

[19] Yasser MH. Bond strength in battened composite columns. Journal of Structural Engineering, 1991, 117(3):699-714.

[20] Roeder CW, Cameron B, Brown CB. Composite action in concrete filled tubes. Journal of Structural Engineering, 1999,125(6):477-484.

[21] Aly A, Elchalakani M, Thayalan P, Patnaikunia I. Incremental collapse threshold for pushout resistance of circular concrete filled steel tubular columns. Journal of Constructional Steel Research, 2020, 66(1):11-18.

[22] Qu, X, Chen Z, Nethercot DA, Gardner L, Theofanous M. Push-out tests and bond strength of rectangular CFST columns. Steel and Composite Structures, 2015, 19(1):21-41.

[23] Chen LH, Dai JX, Jin QL, Chen LF, Liu XL. Refining bond–slip constitutive relationship between checkered steeltube and concrete. Construction and Building Materials, 2015, 79:153-164.

[24] Tao Z, Song TY, Uy B, Han LH. Bond behavior in concrete-filled steel tubes. Journal of Constructional Steel Research, 2016, 120:81–93.

[25] Chen Y, Feng R, Shao YB, Zhang XT. Bond-slip behaviour of concrete-filled stainless steel circular hollowsection tubes. Journal of Constructional Steel Research, 2017, 130:248-263.

[26] Feng R, Chen Y, He K, Wei JG, Chen BC, Zhang XT. Push-out tests of concrete-filled stainless steel SHS tubes. Journal of Constructional Steel Research, 2015, 145:58–69.

[27] Dong HY, Chen XP, Cao WL, Zhao YZ. Bond behavior of high-strength recycled aggregate concrete-filled largesquare steel tubes with different connectors. Engineering Structures, 2020, 211:110392

[28] Dai P, Yang L, Wang J, Fan JW, Lin MF. Experimental study on the steel–concrete bond behaviour of circularconcrete-filled stainless steel tubes. Thin-Walled Structures, 2021, 169:108506.

[29] Li W, Chen B, Han LH, Packer JA. Pushout tests for concrete-filled double skin steel tubes after exposure to fire. Thin-Walled Structures, 2022, 176:109274.

[30] Abendeha RM, Salmana D, Louzi RA. Experimental and numerical investigations of interfacial bond in self-compacting concrete-filled steel tubes made with waste steel slag aggregates. Developments in the Built Environment, 2022, 11:100080

[31] Han LH, Xu CY, Hou C. Axial compression and bond behaviour of recycled aggregate concrete-filled stainless steel tubular stub columns. Engineering Structures, 2022, 262:114306.

[32] Colegrove PA, Coules HE, Fairman JL, Martina F, Kashoob T, Mamash H, Cozzolino LD. Microstructure and residual stress improvement in wire and arc additively manufactured parts through high-pressure rolling. Journal of Materials Processing Technology, 2013, 213:1782-1791.

[33] Haden CV, Zeng G, Carter III FM, Ruhl C, Krick BA, Harlow DG. Wire and arc additive manufactured steel: Tensile and wear properties. Additive Manufacturing, 2017, 16:115-123.

[34] Müller J, Grabowski M, Müller C, Hensel J, Unglaub J, Thiele K, Kloft H, Dilger K. Design and parameter identification of wire and arc additively manufactured (WAAM) steel bars for use in construction. Metals, 2019, 9(7):1-19.

[35] Guo NN, Leu CM. Additive manufacturing: technology, applications and research needs, Frontiers of Mechanical Engineering, 2013, 8(3):215-243.

[36] Laghi V, Palermo M, Gasparini G, Girelli VA, Trombetti T. Experimental results for structural design of wire-and-arc additive manufactured stainless steel members. Journal of Constructional Steel Research, 2020, 16:105858.

[37] Gardner L. Metal additive manufacturing in structural engineering review, advances, opportunities and outlook. Structures, 2023, 47:2178-2193.

[38] Zhao Y, Chen Y, Wang Z, Ye J, Zhao WJ. Mechanical properties, microstructural characteristics and heat treatment effects of WAAM stainless-steel plate material. Journal of Building Engineering, 2023, 75:106988.

[39] Guo X, Kyvelou P, Ye J, Teh LH, Gardner L. Experimental investigation of wire arc additively manufactured steel single-lap shear bolted connections. Thin-Walled Structures, 2022, 181:110029.

[40] Guo X, Kyvelou P, Ye J, Teh TH, Gardner L. Experimental study of DED-arc additively manufactured steel double-lap shear bolted connections. Engineering Structures, 2023, 281: 115736.

[41] Ye J, Liu YY, Yang Y, Wang Z, Zhao O, Zhao Y. Testing, analysis and design of wire and arc additively manufactured steel bolted connections. Engineering Structures, 2023, 296:116939.

[42] Liu YY, Ye J, Yang YZ, Quan G, Wang Z, Zhao W, Zhao Y. Experimental study on wire and arc additively manufactured steel double-shear bolted connections. Journal of Building Engineering, 2023, 76:107330.

[43] Joosten SK. Printing a stainless steel bridge: An exploration of structural properties of stainless steel additive manufactures for civil engineering purposes (Docter Thesis), Delft University of Technology, 2015.

[44] Bolderen GSV, Exploration of stability of 3D-printed steel members (Master Thesis). Delft University of Technology, 2017.

[45] GB (Chinese Code). Code for design of steel structures. GB 50017. Beijing, China:Standards Press of China, 2017.

[46] AISC. Specification for structural steel buildings. AISC360-16. Chicago, USA:AISC, 2016.

[47] CEN. Eurocode 3:Design of steel structures. Part 1.8: design of joints. EN1993-1-8. Brussels, Belgium:CEN, 2007.
[48] AS. Building code of Australia primary referenced standard: steel structures. AS4100. Homebush, Australia:AS, 1998.
[49] Huang C, Kyvelou P, Zhang R, Britton TB, Gardner L. Mechanical testing and microstructural analysis of wire arc additively manufactured steels. Materials and Design, 2022, 216:110544.
[50] Huang C, Kyvelou P, Gardner L. Stress–strain curves for wire arc additively manufactured steels. Engineering Structures, 2023, 279:115628.
[51] Laghi V, Palermo M, Gasparini G, Trombetti T. Computational design and manufacturing of a half–scaled 3D–printed stainless steel diagrid column. Additive Manufacturing, 2020, 36:101505.
[52] Meng X, Weber B, Nitawaki M, Gardner L. Optimisation and testing of wire arc additively manufactured steel stub columns. Thin–Walled Structures, 2023, 189:110857.
[53] Bruggi M, Laghi V, Trombetti T. Simultaneous design of the topology and the build orientation of wire–and–arc additively manufactured structural elements. Computers and Structures, 2021, 242: 106370.
[54] Feucht T, Waldschmitt B, Lange J, Erven M. Additive manufacturing of a bridge in situ. Steel Construction, 2022, 15(2):100–110.
[55] Ye J, Kyvelou P, Gilardi F, Lu H, Gilbert M, Gardner L. An end–to–end framework for the additive manufacture of optimized tubular structures. IEEE Access, 2021, 9:165476–165489.
[56] Lu HJ, He L, Gilbert M, Gilardi F, Ye J. Design of optimal truss components for fabrication via multi-axis additive manufacturing. Computer Methods in Applied Mechanics and Engineering, 2023, 418:116464.
[57] Ye J, Guo QC, Lu HJ, Kyvelou P, Zhao Y, Gardner L, Xie YM. Topology optimisation of self-supporting structures based on the multi-directional additive manufacturing technique. Virtual and Physical Prototyping, 2023, 18(1):2271458.
[58] Yan JJ, Chen MT, Quach WM, Yan M, Young B. Mechanical properties and cross-sectional behavior of additively manufactured high strength steel tubular sections. Thin-Walled Structure, 2019, 144:106158.
[59] Derazkolaa HA, Khodabakhshib F, Gerlichc AP. Fabrication of a nanostructured high strength steel tube by friction-forging tubular additive manufacturing (FFTAM) technology. Journal of Manufacturing Processes, 2020, 58:724-735.
[60] Guo X, Kyvelou P, Ye J, Gardner L. Experimental investigation of wire arc additively manufactured steel T-stub connections. Journal of Constructional Steel Research, 2023, 211:108106.
[61] Chen J, Song SS, Ye J, Quan G, Kyvelou P, Gardner L. Axial compressive behaviour and design of concrete-filled wire arc additively manufactured steel tubes. Structures, 2023, (submitted).

[62] Song SS, Chen J, Quan G, Ye J. Numerical analysis and design of concrete-filled wire arc additively manufactured steel tube under axial compression. Engineering Structures, 2023, (submitted).

[63] Xu F, Chen J, Jin WL. Experimental investigation of thin-walled concrete-filled steel tube columns with reinforced lattice angle. Thin-Walled Structures, 2014, 84:59-67.

[64] Xu F, Chen J, Guo Y and Ye Y. Innovative design of the world's tallest electrical transmission towers. Proceedings of the Institution of Civil Engineers – Civil Engineering 2019, 172(5):9–16.

[65] CEN. Eurocode 4: Design of composite steel and concrete structures-Part 1-1:General rules and rules for buildings. EN1994-1-1. Brussels, Belgium:CEN, 2004.

[66] AS. Bridge design Part 6:Steel and composite construction. AS 5100. Sydney, Australia:AS.

[67] AIJ (Japanese Code). 1997. Recommendations for design and construction of concrete filled steel tubular structures. AIJ. Japan:AIJ, 2004.

[68] Rhinoceros 3D, Robert McNeel & Associates, 2017.

[69] Geomagic Wrap, 3D Systems Inc, 2017.

[70] GB (Chinese Code). Metallic materials-Tensile testing-Part 1: Method of test at room temperature. GB/T 228.1. Beijing, China:Standards Press of China, 2010.

[71] GB (Chinese Code). 2002. Test method for mechanical properties of ordinary concrete. GB/T 50081. Beijing, China:Standards Press of China.

[72] Song SS, Liu X, Chen J, Ye CH, Liu JDR, Liu CB. Compressive behaviour of corroded thin-walled circular section steel stub columns. Thin-Walled Structures, 2022, 180:109794.

[73] Song SS, Xu F, Chen J, Qin FJ, Huang Y, Yan X. Feasibility and performance of novel tapered iron bolt shear connectors in demountable composite beams. Journal of Building Engineering, 2022, 53:104528.

Notation

The following symbols are used in this paper:

Latin upper case letters

A = the average cross-section area of WAAM steel component;

A_i = the cross-sectional area of each contour spacing for the WAAM steel tube;

A_{max} = the maximum cross-section area of WAAM steel component;

A_{min} = the minimum cross-section area of WAAM steel component;

A_s = the cross-sectional area of the WAAM steel tube;

A_{sd} = the standard deviation of the cross-section area;

$A_{\text{Scan,T}}$ = the average cross-sectional area of the WAAM steel tube determined by laser scans;

$A_{\text{Scan,C}}$ = the average area of the typical cross-section of the WAAM tensile coupon determined by laser scans;

C_h = the outer perimeter of the WAAM steel tube determined by hand measurement;

D = the average outer diameter of the WAAM steel tube;

D_h = the average outer diameter of the WAAM steel tube determined by hand measurement;

D_n = the nominal outer diameter of the WAAM steel tube;

D_{Scan} = the average outer diameter of the WAAM steel tube determined by laser scans;

E_c = the elastic modulus of concrete being used;

E_s = the elastic modulus of WAAM steel being used;

L = the average length of the WAAM steel tube;

L_e = the interface length of the push-out specimen;

L_h = the average length of the WAAM steel tube determined by hand measurement;

L_n = the nominal length of the WAAM steel tube;

L_o = 300, the reference length of the CFST specimen;

L_{Scan} = the average length of the WAAM steel tube determined by laser scans;

N_u = the peak load of the push-out specimen obtained in the experiments;

$N_{\text{u\_2\%}}$ = the residual load when the slip reaches 2% of the interface length L_e at the post-peak segment;

S_u = the slip corresponding to the peak load of the push-out specimen;

T = the average thickness of WAAM steel tube;

T_h = the average thickness of the WAAM steel tube determined by hand measurement;

T_n = the nominal thickness of the WAAM steel components;

T_{Scan} = the average thickness of WAAM steel tube determined by laser scans;

T_y = the thickness of the printed layer;

$V_{Hand,T}$ = the volume of the WAAM steel tube determined by hand measurement;

$V_{Scan,T}$ = the volume of the WAAM steel tube determined by 3D laser scans;

$V_{Scan,C}$ = the volume of the WAAM tensile coupon determined by 3D laser scans;

Latin lower case letters

b_n = the nominal width of WAAM steel coupon;

b_{Scan} = the width of WAAM steel coupon determined by 3D laser scans;

f_c = the cylinder compressive strength of concrete being used;

f_{cu} = the cubic compressive strength of concrete being used;

f_y = the yield strength of steel being used;

f_u = the ultimate strength of WAAM steel being used;

$m_{Hand,T}$ = the weight of the WAAM steel tube;

$m_{Hand,C}$ = the weight of the WAAM tensile coupon;

n = the number of contour spacing;

t = the time of the WAAM process;

t_n = the nominal thickness of WAAM steel coupon;

t_{Scan} = the thickness of WAAM steel coupon determined by 3D laser scans;

v_1, v_2 = the welding speed of the WAAM process;

Greek case letters

Δl_1, Δl_2 = the welding arc length of the WAAM process;

ρ = the density of the WAAM steel element;

σ_L = the longitudinal stress of the WAAM steel tube;

τ_0 = the criterion bond stress of the concrete-filled WAAM steel tube;

τ_u = the average bond stress of the concrete-filled WAAM steel tube;

$\tau_{u\_2\%}$ = the residual bond stress when the slip reaches 2% of the interface length L_e at the post-peak segment;

$\tau_{u,AIJ}$ = the predicted bond strength of CFST specimen in AIJ;

$\tau_{u,AISC}$ = the predicted bond strength of CFST specimen in AISC 360-16;

$\tau_{u,AS}$ = the predicted bond strength of CFST specimen in AS 5100;

$\tau_{u,Design}$ = the design bond strength calculated by the proposed approach;

$\tau_{u,EC4}$ = the predicted bond strength of CFST specimen in EC4;

$\tau_{u,Exp}$ = the bond strength of the CFST specimen obtained in the experiments;

ε_L = the longitudinal strain of the WAAM steel tube;

ε_u = the fracture strain of WAAM steel being used;

ε_θ = the transverse strain of the WAAM steel tube;

μ_s = the Poisson's ratio of the WAAM steel tube;

ζ_{su} = the factor of surface undulation for the WAAM steel tube.